Correspondence to:
X. Li,
xuefang.li@uliege.be

Numerical Insights Into the Effects of Model Geometric Distortion in Laboratory Experiments of Urban Flooding

Xuefang Li[1] [ID], **Sébastien Erpicum[1]** [ID], **Emmanuel Mignot[2]** [ID], **Pierre Archambeau[1]** [ID], **Nicolas Rivière[2]**, **Michel Pirotton[1]**, and **Benjamin Dewals[1]** [ID]

[1]Hydraulics in Environmental and Civil Engineering (HECE), University of Liège (ULiège), Liège, Belgium, [2]LMFA, CNRS-Université de Lyon, INSA de Lyon, Lyon, France

Abstract Geometrically distorted scale models have been a valuable tool for physical modeling of urban flooding in a network of streets. However, little is known so far about the bias induced in such cases by the model geometric distortion. Here, we use 2-D computational modeling to provide a first systematic quantification of this bias in the case of a synthetic urban layout. The bias is found to be generally small, with the maximum deviations of the upscaled flow depth and discharge partition from the corresponding values of the undistorted model being around 10% in the case of relatively rapid and shallow flow conditions. When the geometric distortion is increased, the computations reveal a nonmonotonous pattern of the flow variables (depth, discharge partition, and size of flow separation zones), which results from a competition between declining frictional losses and growing local losses in the model. These findings may guide the design of distorted scale models of urban flooding and assist the interpretation of laboratory observations for assessing flood protection measures, for process understanding or for validating computational modeling.

Plain Language Summary Data from laboratory experiments are a valuable complement to field observations for validating flood risk management tools. Recent studies of urban flooding in a network of streets have used geometrically distorted scale models (i.e., involving distinct horizontal and vertical scale factors). This geometric distortion may lead to biases such as alteration of flow regime and of flow structures. Here, we use computational modeling to present a systematic quantitative analysis of the biases induced by geometric distortion in laboratory models of urban flooding.

1. Introduction

1.1. Need for Validation Data

Urban flood risk is increasing worldwide as a result of environmental changes such as more frequent hydro-climatic extremes and due to rapid urbanization (Chen et al., 2015; Hettiarachchi et al., 2018; National Academies of Sciences Engineering and Medicine, 2019). Accurate and reliable tools are critically needed for managing this risk and enhancing flood resilience (Liu et al., 2018; Zhou et al., 2018). Such tools rely on numerical models for computing flood hazard and flood risk. However, the accuracy and applicability of these models still remain hampered by a lack of suitable validation data (Teng et al., 2017; Wang et al., 2018).

While this lack of data also applies to the vulnerability part of flood risk (e.g., Di Baldassarre et al., 2018), we focus here on the hazard component. In most cases, field-scale data of urban flooding are limited to information on inundation extent and estimates of maximum water levels obtained from flood marks, for example, on building walls or bridge piers, whereas conventional remote sensing techniques do not provide data with sufficient spatiotemporal resolution for validating numerical models of urban flooding (Leitão et al., 2018). Consequently, various model settings can perform apparently well when tested against such sparse and uncertain reference data, which usually do not even provide the time when the peak is reached. This leads to equifinality issues; that is, multiple parametrizations of the models lead to acceptable model predictions in the light of limited available calibration and validation data (Beven, 2006). To address this, validation data comprising discharge partitioned between streets in urbanized areas and flow velocity are important. This is particularly true as flow velocity directly influences damage (Molinari & Scorzini, 2017), contaminant transport, scour, and danger for pedestrians and vehicles (Arrighi et al., 2017; Xia et al., 2014).
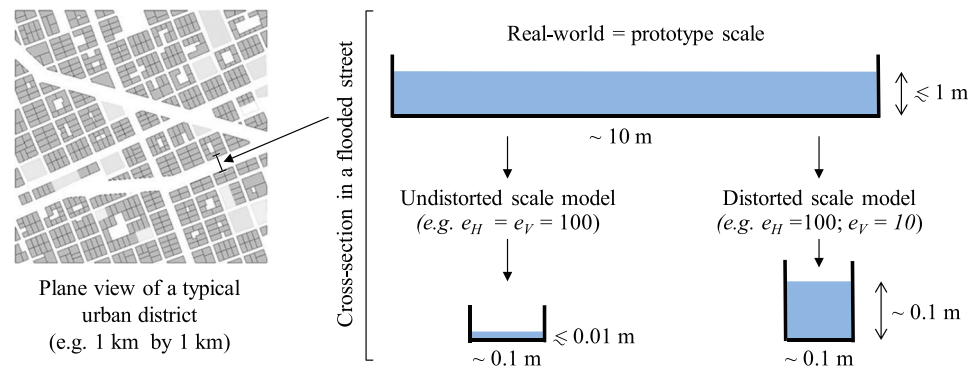
Figure 1. Sketch of geometrically undistorted versus distorted laboratory-scale models of urban flooding.

Recent advances in remote sensing techniques (McCabe et al., 2017) and crowd-sourced data (Jongman, 2018; Wang et al., 2018) offer a new potential for evaluating urban flooding models; but so far mostly the flooding extent has been evaluated using these methods, without accurate validation of the flow field (Yu et al., 2016). In a street in central Brisbane (Australia), during the January 2011 flood, Brown and Chanson (2012, 2013) collected point measurements of turbulent velocity data (at 50 Hz) using acoustic Doppler velocimetry. Data were processed with a triple decomposition, highlighting fluctuations triggered by local topographic effects. Recently, Leitão et al. (2018) applied a method based on large-scale particle image velocimetry to estimate mean flow velocity fields from nonconventional data such as traffic and surveillance camera footages (Macchione et al., 2019; Moy de Vitry et al., 2017). The growing use of unmanned aerial vehicles seems also promising to deliver data sets on surface flow fields during flooding events (Perks et al., 2016).

While field work offers the considerable advantage of giving direct access to data at the real-world scale, that is, there is no issue with upscaling nor potential scale effects, it remains challenging to perform field data collection under flood conditions as well as to interpret these data. Besides involving risks for field data collection workers (Muste et al., 2008), field measurements are conducted in uncontrolled, complex real-world configurations and substantial uncertainties remain regarding the proper identification of boundary conditions and the velocity distribution over the flow depth. Moreover, conventional sensors are imperfectly suited to urban environments, where they face risk of vandalism and may be expensive to maintain and repair (Leitão et al., 2018).

Consequently, laboratory experiments may provide a valuable complement to field data to achieve reliable validation of flood hazard models. Provided that appropriate flow scaling is ensured, laboratory experiments allow detailed and accurate measurements under controlled flow conditions (Mignot et al., 2019). Measurements options include flow depth, flow discharge, velocity field in 2-D and 3-D for various urban flood configurations, such as street intersections (Creëlle et al., 2018; Mignot et al., 2013; Rivière et al., 2011), exchanges between drainage system and surface flow (Fraga et al., 2017; Lopes et al., 2017; Martins et al., 2017; Rubinato et al., 2017), flow through groups of obstacles (Testa et al., 2007; Velickovic et al., 2017), and flow in realistic urban districts (Finaud-Guyot et al., 2018; Güney et al., 2014; Smith et al., 2016).

1.2. Multiscale Nature of Urban Flooding

Urban flooding is a genuinely multiscale process, with the typical extent of an urban district being 10^2 to 10^4 m, whereas the corresponding flow depths of interest are of the order of 10^{-2} to 1 m (Li et al., 2019). Designing a laboratory-scale model using the same scaling along the horizontal and vertical directions would frequently result in millimeter-scale flow depths in the scale model (Figure 1), which would lead to measurement difficulties and lack of representativeness due to viscous and capillary effects (Ishigaki et al., 2003), or in a giant experimental setup which could hardly be accommodated in most hydraulic laboratories.

To address this issue, recent experimental research on urban flooding used different scale factors along the horizontal and vertical directions, resulting in geometrically *distorted* scale models (Finaud-Guyot

et al., 2018; Güney et al., 2014; Lipeme Kouyi et al., 2010; Smith et al., 2016). The horizontal scale factor e_H is defined as the ratio between a horizontal length in the prototype and the corresponding length in the model, and the vertical scale factor e_V is defined in a similar way for the vertical dimensions. Therefore, a relatively large value of e_H is used to limit the extent of the laboratory setup while keeping relatively high flow depths thanks to a smaller value of e_V (Figure 1). This strategy is expected to improve the accuracy and representativeness of the measurements (Arndt et al., 2000; Li et al., 2019).

1.3. Geometrically Distorted Hydraulic Models

Distorted models have been used for a broad range of applications in fluvial, estuarine, and coastal hydraulics given the multiple benefits they offer, both from the economical point of view (since relatively large values of e_H reduce the construction costs) and from a technical perspective (improved relative accuracy of the flow depth measurements, less pronounced viscosity and capillary effects). In particular, keeping the influence of surface tension effects insignificant requires usually a minimum water depth of 0.015 to 0.030 m (Novak et al., 2010). These critical values are reached more easily in a geometrically distorted model.

One of the most notable examples of distorted hydraulic models is the outdoor 1.5-km by 2-km model of the Mississipi river (3,800 km long) built by the U.S. Army Corps of Engineers using a vertical scale factor $e_V = 100$, which is 20 times lower than the horizontal one $e_H = 2,000$ (Chanson, 1999; Henderson, 1966). Novak et al. (2010) describe a laboratory-scale model of river Dargle in the town of Bray (Ireland) built with $e_H = 100$ and $e_V = 50$ ($e_H/e_V = 2$) to assess the performance of flood mitigation measures for various tidal events. Jung et al. (2012) used $e_H = 120$ and $e_V = 50$ ($e_H/e_V = 2.4$) to study the effect of a floating island in a river, while Wakhlu (1984) obtained comparable results in an undistorted ($e_H = e_V = 36$) and a distorted model ($e_H = 100$ and $e_V = 17$) of a river division weir.

In estuary models, scale distortion is almost the norm given the substantial extent of the areas to be covered. Ratios e_H/e_V of the order of 10 are not unusual (Novak et al., 2010). Among others, a model of a 35-km-long section of the Seine estuary was built at Sogreah laboratory (Grenoble) with $e_H = 1,000$ and $e_V = 100$ ($e_H/e_V = 10$) in the framework of an extension of Le Havre harbor (Port 2000 scheme). However, Sharp and Khader (1984) found distortion effects by comparing an undistorted ($e_H = e_V = 20$) and a distorted model ($e_H = 400$ and $e_V = 100$) of a harbor in a study of wave transmission and stone stability assessment.

For models of rivers and floodplains, Chanson (1999) suggests that geometric distortion usually gives good results provided that the ratio e_H/e_V remains below 5 to 10. Nevertheless, little is known about the quantitative impacts of model geometric distortion on flow processes governing urban flooding. Compared to the case of an undistorted scale model, the model geometric distortion alters the relative importance of inertia and viscous forces, and it eventually affects the influence of friction. Moreover, the aspect ratio of the flow cross section (depth to width ratio) can be altered significantly by the distortion (Figure 1), so that the development of 2-D and 3-D turbulent flow structures is likely to be affected (Chu & Babarutsi, 1988). The resulting effect of all these factors on the flow variables (flow depth and velocity, and discharge partition) is uncertain. Previous studies on the effect of geometric distortion focused mostly on very different flow types compared to the present study, for example, flow on hydraulic structures (Heller, 2011; Wakhlu, 1984), with the exception of Li et al. (2019), who highlighted the effects of model geometric distortion in the case of urban flooding. However, their data set was limited and general conclusions could not be drawn.

1.4. Research Objective

In the present study, we aim at providing for the first time a systematic quantitative analysis of the effects of geometric distortion on scale modeling of urban flooding, as well as attributing these effects to specific flow processes.

Since no comprehensive laboratory data set exists so far for this purpose, we opted for 2-D computational modeling to investigate the effects of flow regime change, the alteration of relative roughness and the influence of flow aspect ratio. Although 2-D computations "do not tell the whole story" (e.g., regarding form drag, secondary currents, and 3-D flow structures), we believe that they deliver valuable information given the present state of knowledge. Indeed, although secondary currents are not reproduced, 2-D simulations account for local flow contractions, changes in discharge partition in-between streets, and friction on the bottom and on the sidewalls. Moreover, opting for 2-D modeling is a pragmatic choice as it allows

conducting a large number of model runs (~100 in this study) with reasonable computational cost. Part of the value of our results stems from the systematic comparison among the outcomes of many computations in various settings. Conversely, Ramos et al. (2019) pointed out recently that a high mesh resolution remains necessary for 3-D computations to capture secondary flows. As a consequence, conclusions requiring systematic comparisons could not have been reached based on a limited number of high-resolution 3-D simulations. Finally, our results have the merit of revealing the most intriguing cases for specific configurations that should be simulated in 3-D in future research.

For the case of a synthetic simplified urban district, we perform 2-D computational modeling to compare flow variables, such as flow depths, discharge partition, and the extent of flow separation zones, obtained by simulations with various horizontal scale factors and geometric distortions. This allows quantifying the deviations between the results of the prototype-scale simulations (considered as a reference) and those derived by upscaling the outputs of simulations mimicking various laboratory-scale models.

In section 2, we present a dimensional analysis, which highlights the governing parameters for urban flooding in a network of streets and supports the systematic analysis conducted hereafter. Next, the computational model and the synthetic urban district are introduced in section 3. The main results are presented in section 4. In section 5, we discuss how the effects of model geometric distortion are related to basic flow processes, partly based on power balance analysis. Section 6 further discusses the results and provides recommendations for designing urban flooding experiments, while conclusions are drawn in section 7.

2. Dimensional Analysis

Urban flooding in a network of streets may be described by $n = 8$ dimensional parameters, namely a typical street width b, a characteristic discharge Q_0, a characteristic flow depth h_0, the gravity acceleration g, the water density ρ and kinematic viscosity ν, a roughness height k_s, and the surface tension σ (Table S1 in the supporting information). These parameters involve $p = 3$ dimensions (mass $[M]$, length $[L]$, and time $[T]$). Therefore, $n - p = 5$ independent dimensionless parameters can be defined. As detailed in Table S1, all studied variables, expressed in dimensionless form (noted y), can be expressed as a function of five dimensionless parameters:

$$y = f\left(\frac{h_0}{b}, F_0, R_0, \frac{k_s}{h_o}, W_0\right) \tag{1}$$

with $F_0 = Q_0/[b\, h_0\, (g\, h_0)^{1/2}]$ the Froude number, $R_0 = 4\, Q_0/\,(b\, \nu)$ the Reynolds number, k_s/h_0 the relative roughness, and $W_0 = \rho\, (Q_0/b)^2/(\sigma\, h_0)$ the Weber number. These parameters represent, respectively, the relative importance of the gravity force, the viscous forces, the bottom roughness, and the surface tension. The generic notation y may refer particularly to a dimensionless flow depth h/b (e.g., upstream of the urban network) or a discharge ratio reflecting the flow partition in-between streets. Equation 1 applies whatever the considered scale, either prototype or laboratory model.

In this study, we aim at analyzing the influence of the model scaling (including geometric distortion) on the flow observed in a virtual laboratory model, for various flooding scenarios. Therefore, it is of relevance to reformulate Equation 1 so that the parameters related to model scaling and those defining the flooding scenario appear explicitly:

1. The model *scale* is defined through the horizontal and vertical scale factors e_H and e_V.
2. A flooding *scenario* is defined here at the prototype scale, by setting the value of the characteristic discharge Q_0, flow depth h_0, and roughness height k_s for a given urban geometry (with a typical street width b). Based on these values and the properties of water (viscosity, surface tension), it is hence possible to set the value of the five dimensionless numbers introduced in Equation 1: $h_{0,p}/b_p$, $F_{0,p}$, $R_{0,p}$, $k_{s,p}/h_{0,p}$, and $W_{0,p}$, where subscript "p" refers to the real-world prototype scale. As detailed by Li et al. (2019) and Heller (2011), as well as in textbooks (Arndt et al., 2000; Chanson, 2004), laboratory-scale modeling of free surface flow is generally based on Froude similarity. This means that the scaling of flow velocity is related to the geometric scaling, by considering $F_{0,m} = F_{0,p}$, with subscript "m" referring to the model scale. By applying Froude similarity, we can express any dimensionless quantity y_m at the laboratory scale as

$$y_m = f\left(\frac{h_{0,m}}{b_m}, F_{0,m}, R_{0,m}, \frac{k_{s,m}}{h_{0,m}}, W_{0,m}\right) = f\left(\frac{h_{0,p}e_H}{b_p \, e_V}, F_{0,p}, R_{0,p} \frac{\nu_p/\nu_m}{e_V^{3/2}}, \frac{k_{s,p}}{h_{0,p}} \frac{k_{s,m}}{k_{s,p}/e_V}, W_{0,p} \frac{(\rho_p\sigma_p)/(\rho_m\sigma_m)}{e_V^2}\right) \quad (2)$$

Introducing the distortion ratio $d = e_H/e_V$ to quantify the model geometric distortion, Equation 2 becomes

$$y_m = f\left(\frac{h_{0,p}}{b_p}d, F_{0,p}, R_{0,p} \frac{(\nu_p/\nu_m)d^{3/2}}{e_H^{3/2}}, \frac{k_{s,p}}{h_{0,p}} \frac{k_{s,m}}{k_{s,p}/(e_H/d)}, W_{0,p} \frac{(\rho_p\sigma_p)/(\sigma_m\rho_m)d^2}{e_H^2}\right) \quad (3)$$

Equation 3 shows that the laboratory observations y_m depend on four groups of parameters:

3. the five parameters $h_{0,p}/b_p$, $F_{0,p}$, $R_{0,p}$, $k_{s,p}/h_{0,p}$, and $W_{0,p}$, reflecting "which real-world flooding scenario is being studied";
4. parameters e_H and d, which reflect the *decisions made by the modeler* in terms of model geometric scaling;
5. ratio $k_{s,m}/[(k_{s,p}/(e_H/d)]$, resulting from the choice of the bed material in the scale model;
6. ratios ν_p/ν_m and σ_p/σ_m, reflecting the choice of fluids used to carry out the experiments.

A "perfect" scale model would preserve the same value as in prototype for all five dimensionless parameters, but this is impossible in reality. Indeed, given that in experimental studies of urban flooding in street networks, typical values of e_H range between 30 and 200, whereas d varies between 1 and 10 (Li et al., 2019), a fluid substantially less viscous than water would be needed to ensure $(\nu_p/\nu_m) \, d^{3/2}/e_H^{3/2} = 1$ in Equation 3, so that $R_{0,m} = R_{0,p}$. Additionally, preserving $W_{0,p} = W_{0,m}$ would require to ensure $(\rho_p \, \sigma_p/\rho_m \, \sigma_m) \, d^2/e_H^2 = 1$ (e.g., adding chemicals to adjust σ_m or changing the gas above the free surface), which is a challenging task in experiments. Therefore, in practice, all experimental studies of urban flooding so far have been performed just by using water, without chemical additions and without changes of the gas above the free surface (Mignot et al., 2019). Here, we also assume throughout the study that the fluid in the laboratory models is water, so that Equation 3 reduces to

$$y_m = f\left(\frac{h_{0,p}}{b_p}d, F_p, R_p \frac{d^{3/2}}{e_H^{3/2}}, \frac{k_{s,p}}{h_{0,p}} \frac{k_{s,m}}{k_{s,p}/(e_H/d)}, W_p \frac{d^2}{e_H^2}\right) \quad (4)$$

Note that Equation 4 can also be rewritten as follows:

$$y_m = f\left(\frac{h_{0,p}}{b_p}d, F_p, R_p \frac{d^{3/2}}{e_H^{3/2}}, \frac{k_{s,p}}{h_{0,p}} \frac{k_{s,m}}{k_{s,p}/(e_H/d)}, M_p\right) \quad (5)$$

with the Morton number defined as $M_p = W_p^3/(F_p^2 \, R_p^4) \sim g \, (\rho \, \nu)^4/(\rho \, \sigma^3)$ (Chanson, 1999; Novak et al., 2010). Since the same fluids are considered in the model and in the prototype, M_p remains constant despite the change of scale (Pfister & Chanson, 2012). Hence, with a Froude similarity and given fluids, both viscous and capillary effects are accounted for in Equation 5 by means of the Reynolds number.

Consequently, the dimensionless values y_m corresponding to laboratory-scale observations differ from the corresponding actual values y_p at the prototype scale. Reasons for this are emphasized in Equation 4:

1. the Reynolds number in the model becomes much smaller than at prototype scale, since $R_{0,m} = R_{0,p} \, d^{3/2}/e_H^{3/2} < R_{0,p}$, leading thus to a possible bias due to viscous and capillary effects;
2. to partly compensate for the viscous and capillary effects, the scale model may be geometrically distorted ($d > 1$, permitting to artificially increase the ratios $d^{3/2}/e_H^{3/2}$ and d^2/e_H^2); but this leads in turn to a possible bias due to changes in the aspect ratio of the flow in the streets because in such a case $h_{0,m}/b_m > h_{0,p}/b_p$;
3. depending on the material used for building the street bottom and sidewalls of the laboratory-scale model, $k_{s,m}$ may differ from $k_{s,p}/(e_H/d)$, leading to a possibly biased representation of roughness effects.

The implications of variations of the Reynolds number R_0, relative roughness k_s/h_0 and aspect ratio h_0/b between the prototype and a scale model (with or without geometric distortion) are precisely what we intend to quantify in this study for the case of urban flooding in a network of streets.
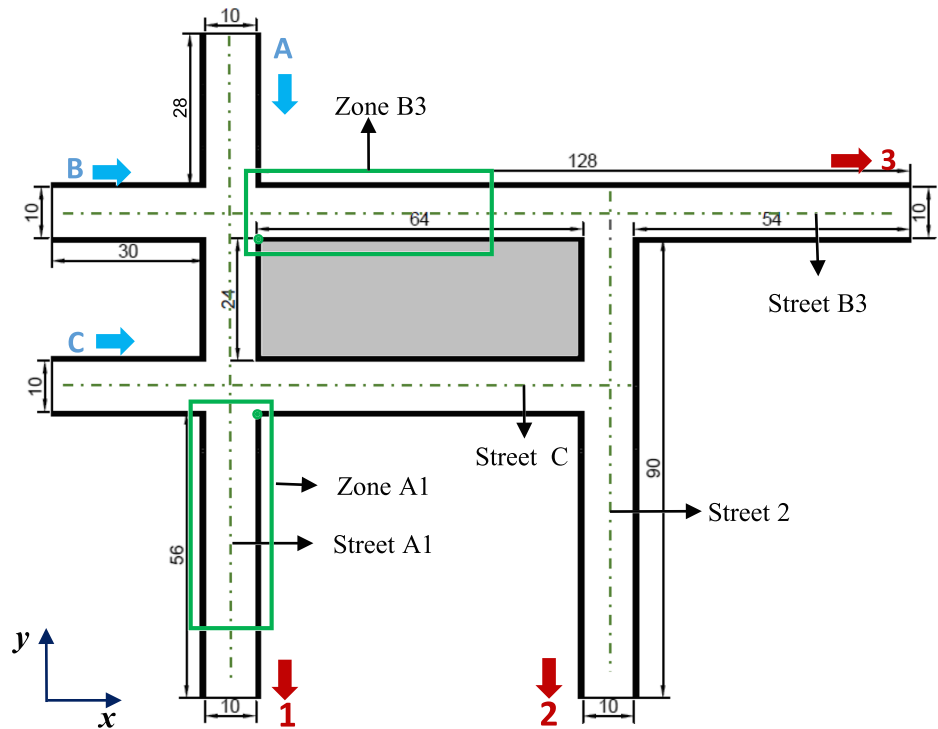
Figure 2. Considered urban layout, representing part of a synthetic urban district. Dimensions (m) at prototype scale.

3. Data and Methods

In this section, we first introduce the geometry of the synthetic urban district considered for the analysis (section 3.1). Next, we briefly describe the computational model used for the numerical simulations (section 3.2) and we present the strategy followed for defining the test program and conducting the simulations (section 3.3).

3.1. Synthetic Urban District

The considered urban layout is shown in Figure 2. It represents a part of an idealized urban district of about 168 m by 130 m at prototype scale. It includes three inlets (labeled A, B, and C) and three outlets (labeled 1, 2, and 3). The street width $b_p = 10$ m is constant and identical for all streets. The bottom is horizontal; hence, the case of flooding in mountain areas with particularly high Froude numbers (e.g., Sturm et al., 2018) is not covered here.

We acknowledge that the choice of the urban layout geometry is arbitrary and that it has certainly an influence on the results of the study. Despite this, the chosen geometry corresponds to a typical setting for a small urban district. It is also purposely simple to facilitate interpretation; but nonetheless, it involves a variety of flow features resulting from the combination of four-branch and three-branch crossroads (involving both flow junctions and divisions).

Moreover, the focus is set here on the study of the influence of the model geometric distortion on flow variables by means of a systematic analysis for various model scales and flooding scenarios. As detailed in section 3.3, this leads to varying a total of four degrees of freedom: two parameters characterizing the flooding scenario ($h_{0,p}/b_p$, $F_{0,p}$), the horizontal scale factor e_H, and the geometric distortion d. Therefore, we did not want to include a substantial amount of additional independent variables characterizing the planform geometry of the urban district (e.g., varying street length, width, curvature, or slope). This should be considered in future work.

In the following, the streets are labeled according to their inlets and outlets: "B3" and "C" for the streets along the x axis and "A1" and "2" for the streets along the y axis.

Table 1
Flooding Scenarios and Corresponding Dimensionless Parameters

	Shallow flooding	Deep flooding
	$h_{0,p}/b_p = 0.05$	$h_{0,p}/b_p = 0.15$
Slow flow $F_{0,p} = 0.2$	Scenario "SS"	Scenario "SD"
Rapid flow $F_{0,p} = 0.6$	Scenario "RS"	Scenario "RD"

3.2. Numerical Model

We used the academic modeling system WOLF developed at the University of Liège. It solves the 2-D shallow-water equations with a finite volume technique on a Cartesian grid. The model equations are detailed in Text S1 (in the supporting information). The effect of turbulence on the mean flow is modeled using the Boussinesq approximation. The eddy viscosity is computed by a depth-averaged k-ε model developed by Erpicum et al. (2009). A Darcy-Weisbach formulation is used to estimate the bed shear stress. The friction coefficient c_f is computed by Colebrook-White formula:

$$\frac{1}{\sqrt{4c_f}} = -2\log_{10}\left(\frac{k_s}{14.8\ h} + \frac{2.51}{R\ \sqrt{4c_f}}\right) \qquad (6)$$

where h is the flow depth computed locally. Both bottom and sidewall friction are taken into account in the friction source terms, through a similar formulation as used by Erpicum et al. (2009) and Erpicum et al. (2010). All model equations were presented in detail by Camnasio et al. (2014). The ability of the model to simulate complex turbulent flow as well as urban flooding was demonstrated in a number of previous studies (Arrault et al., 2016; Bruwier et al., 2017). Intrinsic limitations of 2-D depth-averaged models to deal with form drag and recirculation are discussed in section 6.2.

3.3. Test Program

In the laboratory experiments that we consider, an experimental run is defined by setting, as boundary conditions, the value of the inflow discharge Q_{in} at each of the three inlets A, B, and C and the flow depth h_{out} at each of the three outlets 1, 2, and 3 (Figure 2). To facilitate the interpretation of the results and reduce the number of degrees of freedom, we assume that the same discharge is supplied in the three inlets, and the same flow depth is prescribed at the three outlets.

In a scale model, the value of the inflow discharge Q_{in} and the downstream flow depth h_{out} depends on the prototype-scale flooding scenario to be reproduced experimentally, as well as on the considered scale factors e_H and e_V. Hence, we follow a two-step procedure to elaborate the test program and determine the model boundary conditions Q_{in} and h_{out}:

Step 1: definition of prototype-scale flooding scenarios,
Step 2: selection of scaling parameters (e_H and e_V, or e_H and $d = e_H/e_V$).

The value of the roughness height k_s also needs to be specified, both at prototype scale and in the scale model, as well as the grid refinement.

3.3.1. Prototype-Scale Flooding Scenarios (Step 1)

We introduce two families of scenarios, corresponding respectively to relatively "slow" and "rapid" inundation flows. We also distinguish between scenarios involving relatively "shallow" and "deep" flooding conditions. This leads to four flooding scenarios, labeled "SS," "SD," "RS," and "RD" as detailed in Table 1.

To characterize each of these scenarios in quantitative terms, we refer to the dimensional analysis presented in section 2. Accordingly, a flooding scenario may be specified by setting values for two parameters: the aspect ratio $h_{0,p}/b_p$ and the Froude number $F_{0,p}$. To do so, we introduce a few reasonable assumptions:

1. The prototype-scale flow depth at each outlet is assumed of the order of 0.5 and 1.5 m for the "shallow" and "deep" flooding scenarios, respectively, leading to $h_{0,p}/b_p = 0.05$ and $h_{0,p}/b_p = 0.15$ (Table 1). The considered characteristic flow depth h_0 is the value prescribed at the downstream end of the model: $h_0 = h_{out}$.
2. The Froude number $F_{0,p}$ is set to 0.2 for the "slow" flow scenarios and to 0.6 for the "rapid" flow scenarios (Table 1). We can determine the characteristic flow discharge Q_0 by using $F_{0,p}$ and the previously defined values of $h_{0,p}$, and eventually prescribe this discharge at the model inlets: $Q_0 = Q_{in}$.

Note that here $F_{0,p}$ does not refer to a local value of the Froude number, but instead to a lumped value, which combines the inflow discharge Q_{in} and the flow depth h_{out} at the outlets. Hence, even if the "rapid" scenarios
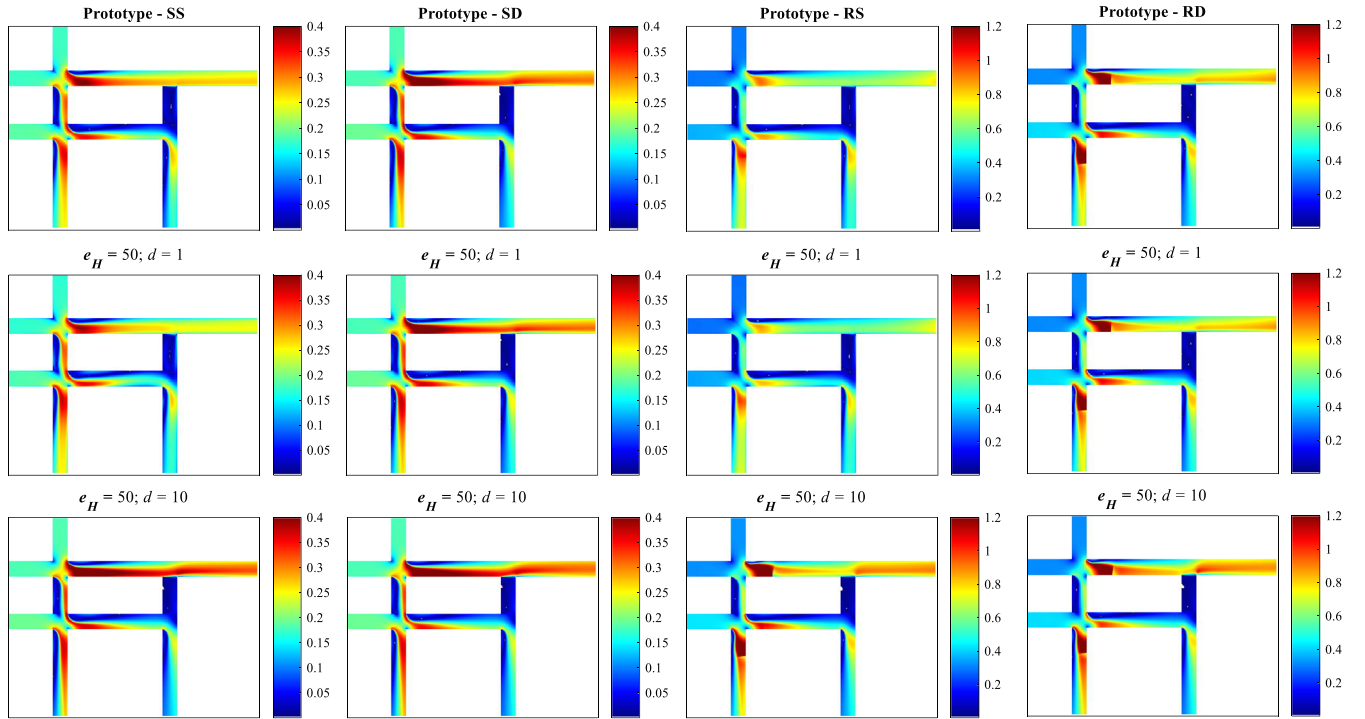
Figure 3. Maps of computed local Froude numbers for the four considered flooding scenarios (SS, RS, SD, and RD), at prototype scale (with $k_{s,p} = 5$ mm) as well as for the horizontal scale factor $e_H = 50$, without and with geometric distortion ($d = 1$ and $d = 10$).

are characterized by $F_{0,p} = 0.6$, there will be substantially higher local values of the Froude number. Indeed, local Froude numbers up to 1.2 are observed in several branches downstream of crossroads in Scenarios RD and RS (Figure 3 and Figure S4 in the supporting information). This is consistent with real-world observations of urban flooding, such as reported by Mignot et al. (2006).

3.3.2. Scaling Parameters (Step 2)

In the following, we intend to compare the computational results obtained at the prototype scale to results of simulations conducted by assuming various values for the horizontal scale factor e_H and for the model geometric distortion (d). In earlier studies of urban flooding in street networks, the horizontal scale factor e_H lies in the range of 30 to 200 (Li et al., 2019). Therefore, we chose here to perform simulations for $e_H = 50$. We also analyzed the sensitivity of our findings to this choice by repeating the simulations of two flooding scenarios (SS and RD) with a smaller ($e_H = 20$) and a higher ($e_H = 100$) value of the horizontal scale factor (section 4). In all cases, we varied the model geometric distortion between $d = 1$ and values up to 15 or even 25. This enables covering the full range of geometric distortion values generally encountered in experimental studies of urban flooding in street networks (Li et al., 2019).

Once the flooding scenarios are specified (through the values of $F_{0,p}$ and $h_{0,p}/b_p$, as shown in Table 1) and the scaling parameters e_H and d are set, it is possible to determine the boundary conditions at the inlets and outlets of the computational domain:

$$Q_{in} = Q_{0,m} = F_m \, b_m \, h_{0,m} \sqrt{g \, h_{0,m}} = F_p \, \frac{b_p}{e_H} \, \sqrt{g} \, h_{0,m}^{3/2} = \sqrt{g} \, b_p^{5/2} \, F_p \, \left(\frac{h_{0,p}}{b_p}\right)^{3/2} \frac{d^{3/2}}{e_H^{5/2}}, \tag{7}$$

$$h_{out} = h_{0,m} = \left(\frac{h_{0,p}}{b_p}\right) d \frac{b_p}{e_H} \tag{8}$$

where the definition of the Froude number: $F_0 = Q_0/[b \, h_0 \, (g \, h_0)^{1/2}]$ was used (section 2). Table S2 (in the supporting information) provides a complete list of all geometric distortions and horizontal scale factors used in the simulations for the four considered flooding scenarios.

Table 2
Grid Spacing Used in the Simulations

Scale	Prototype	$e_H = 20$	$e_H = 50$	$e_H = 100$
Street width (m)	10	0.5	0.2	0.1
Cell size (m)	0.25	0.01	0.005	0.002
Number of cells over each street cross section	40	50	40	50

3.3.3. Bottom and Sidewall Roughness

Since experimental models of urban flooding in street networks are typically constructed with smooth material (e.g., Plexiglas, polyvinyl chloride [PVC], and glass) (Finaud-Guyot et al., 2018; Velickovic et al., 2017), we performed most of the simulations by assuming a roughness height $k_{s,m} = 10^{-5}$ m for the scale models (section 4). Since rough material was also used in some previous studies (Güney et al., 2014; LaRocque et al., 2013; Smith et al., 2016), we also tested the influence of varying this value, as discussed in section 6.1.

3.3.4. Grid Resolution and Convergence in Time

Table 2 summarizes the grid spacing used for the simulations at prototype scale as well as for the three scale models. Note that, in all cases, the number of computational cells over a street width remains above or equal to 40. Grid convergence is further discussed in Text S2 and Figure S1 in the supporting information.

In most simulations, the steady state corresponds to periodically oscillating computed flow variables (flow depths, discharges, and velocity fields). These oscillations are well discretized as their period is substantially higher than the computational time step. They result from fluctuations in the shape of flow separation zones, particularly downstream of the street intersections. However, here, we are primarily interested in the time-averaged results. The time averaging was performed over the N last simulation steps, where N for each case was selected in such a way that the time-averaged variable does not vary anymore with the value of N and remains independent of the transient phase at the beginning of the simulation. The convergence of all the simulations was checked as depicted in Figures S2 and S3 in the supporting information. The standard deviations reflecting the magnitude of the oscillations in time are reported in section 4.

4. Results

In this section, we first provide a general description of the computed flows (section 4.1). Next, we detail the computed flow depths at the inlets and discharge partitions between the outlets (section 4.2). Finally, we analyze the extent of flow separation zones downstream of selected street intersections (section 4.3).

4.1. General Flow Description

Figure 3 shows the spatial distribution of the computed local Froude number $F = \|\mathbf{v}\|/(g\,h)^{0.5}$ (with $\|\mathbf{v}\|$ the magnitude of the local flow velocity and h the computed local flow depth), for the four considered flooding scenarios (SS, RS, SD, and RD), at prototype scale (with $k_{s,p} = 5$ mm) as well as for the horizontal scale factor $e_H = 50$ without and with geometric distortion ($d = 1$ and $d = 10$, respectively). In this section, the roughness height $k_{s,m}$ for all the scale models is 10^{-5} m, which is the typical roughness height of PVC material. Similar results obtained with the horizontal scale factors $e_H = 20$ and $e_H = 100$ are shown in Figure S4 (supporting information).

In the "slow" flow scenarios (SS and SD), the Froude number does not exceed 0.4, whereas for the "rapid" flow scenarios (RS and RD), the flow becomes supercritical ($F \sim 1.2$) in the vena contracta downstream of street intersections (Rivière et al., 2014). This applies both at prototype scale and for the scale models, whatever the geometric distortion and horizontal scale factor (Figure 3 and Figure S4 in the supporting information).

Hence, varying the horizontal scale factor and distortion has a limited impact on the pattern of Froude number, except in the case of the "shallow" flooding scenarios (SS and RS). Indeed, in these cases, the patterns computed for a geometric distortion of 10 deviate substantially from the results obtained at prototype scale and for $d = 1$. This is also reported in quantitative terms in Table S3 (supporting information).

Figures S5 and S6 (supporting information) provide 2-D maps of the computed local Reynolds numbers $R = 4\,h\,\|\mathbf{v}\|/\nu$, while statistical distributions of the Reynolds number are shown in Figure S7. At prototype scale, the Reynolds number is of the order of 10^5–10^7. For the scale models, the Reynolds number drops substantially, especially in the cases without distortion with $e_H = 50$ and $e_H = 100$, in which, respectively, 27.99% and 100% of the Reynolds numbers are below 2,000 for Scenario SS. A geometric distortion of $d = 10$ increases the mean Reynolds number up to a range of $[2.75–7.79] \times 10^4$ (Table S4 in the supporting
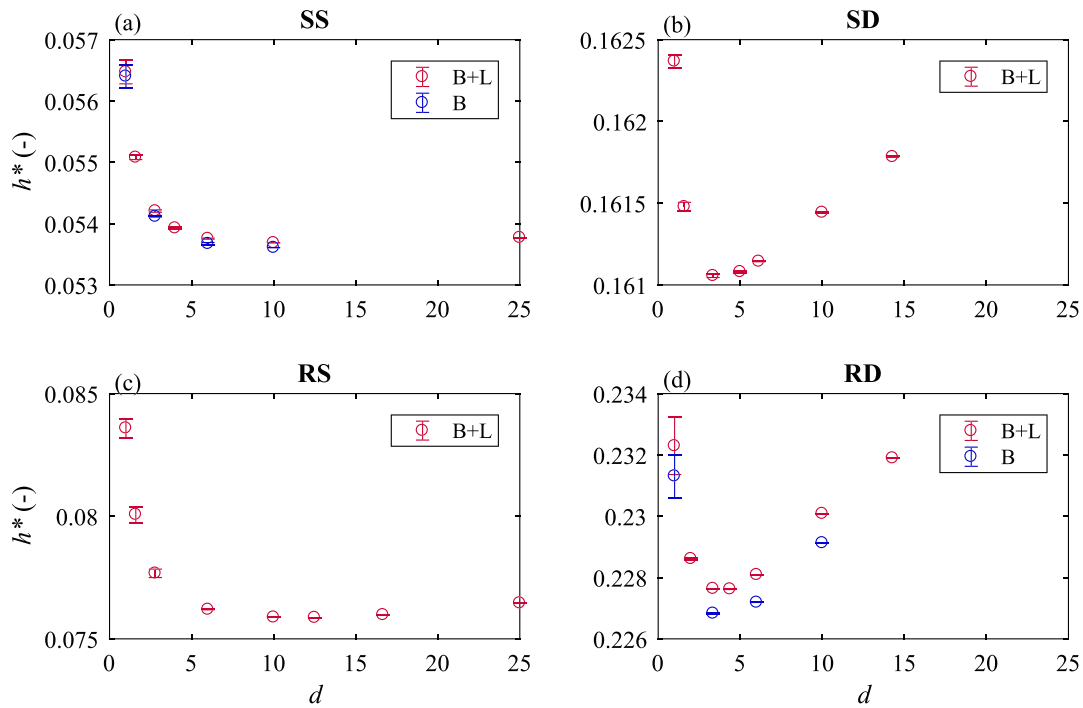
Figure 4. Standardized upscaled flow depth *h** at Inlet A as a function of the model geometric distortion, for a horizontal scale factor $e_H = 50$ and in the (a–d) four considered flooding scenarios. In the legend, "B + L" refers to computational results accounting for bottom and sidewall friction, whereas "B" refers to computations in which only the bottom friction was considered. The error bars show the standard deviation of the time series of the results.

information), while 99.4% and 96.38% of the Reynolds numbers are beyond 2,000 for model $e_H = 50$ and $e_H = 100$, respectively.

4.2. Flow Depths and Discharge Partition

To enable comparison between prototype-scale results and those of different scale models with various values of *d*, we introduce the following standardized flow depth h^*:

$$h^* = \frac{h_m \, e_V}{b_p} = \frac{h_m}{b_m} \frac{1}{d} \tag{9}$$

It corresponds to an upscaling of the scale-model flow depth ($h_m \, e_V$), divided by the prototype-scale street width (b_p). Equivalently, it can be seen as the dimensionless flow depth computed at the laboratory scale (h_m/b_m), divided by the corresponding distortion ratio *d*.

For a horizontal scale factor $e_H = 50$ and the four considered flooding scenarios, Figure 4 shows the standardized flow depth as a function of the distortion ratio, while Figure 5 gives the computed discharge partition between the three outlets. Figure 4 displays only the upscaled flow depths computed at Inlet A, because the results are very similar to those computed at Inlets B and C, as shown in Figure S8 in the supporting information.

The error bars represent the standard deviation of the time-dependent fluctuations in the computed results, as detailed in section 3.3. When comparing the relative size of the error bars in Figure 4, it can be inferred that the effect of flow fluctuations on the upscaled flow depths is magnified when the scale model is undistorted or slightly distorted.

In every scenario and for all model distortions, the largest portion of the inflow discharge ends up in Outlet 3, which is closely connected to Inlets A and B. The second largest portion of discharge is found at Outlet 1, located very close to Inlet C. Outlet 2 receives the smallest portion of discharge.
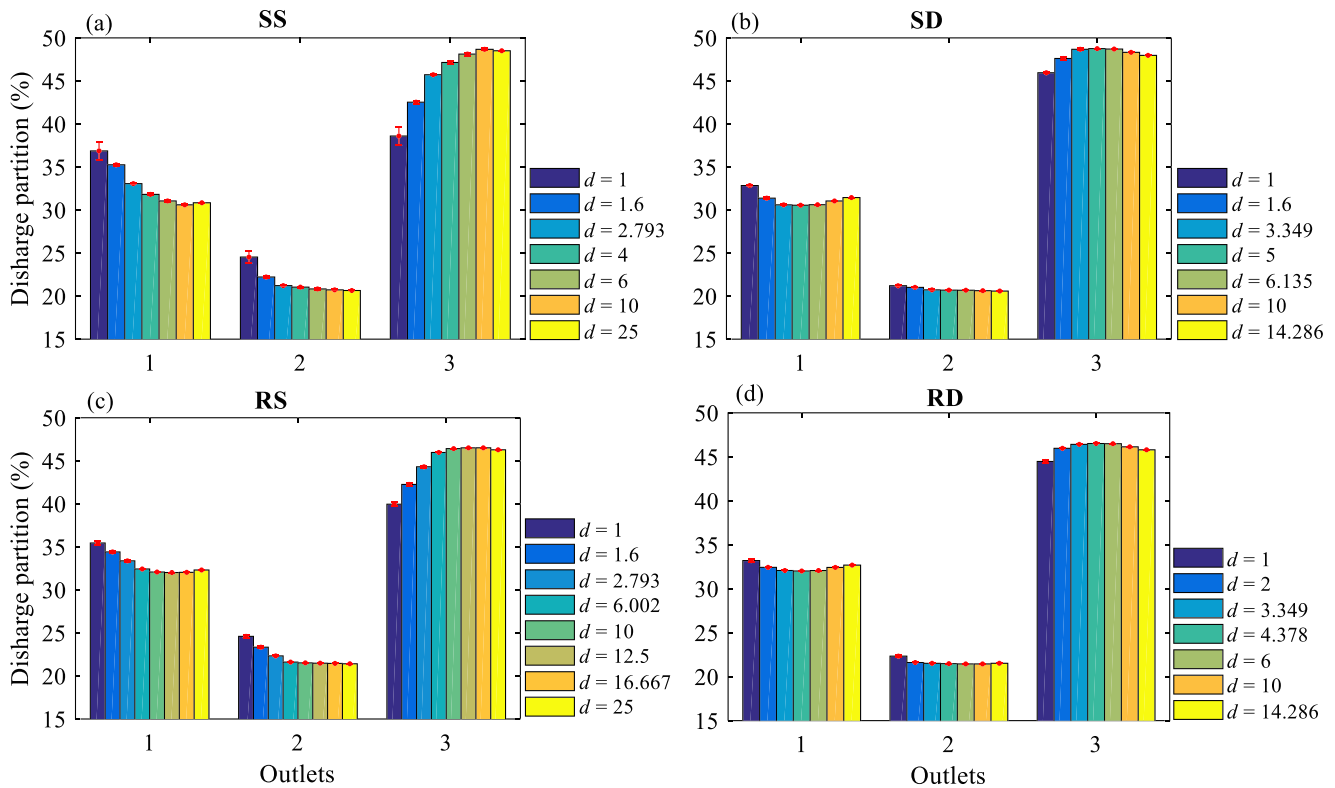
Figure 5. Partition of outflow discharge as a function of the distortion ratio d, for a horizontal scale $e_H = 50$ and the (a–d) four flooding scenarios. The error bars (in red) show the standard deviation of the time series of the computed results.

4.2.1. Magnitude of the Bias Induced by Geometric Distortion

When the geometric distortion ratio varies, the magnitude of the change in the computed standardized flow depth h^* and discharge partition depends on the scenario (Figures 4 and 5). For the "deep" flow scenarios (SD and RD), the maximum effect of geometric distortion does not exceed 1% to 2% of the standardized flow depth and 2 to 3 percentage points in the discharge partition. In contrast, these differences become much more prominent for the "shallow" flow scenarios (SS and RS). Indeed, the effect of geometric distortion on h^* reaches up to 5% in the SS scenario and even 10% for the RS scenario. The influence on the discharge partition is of the order of 6 to 10 percentage points for scenarios SS and RS at Outlets 1 and 3. At Outlet 2, the variation of discharge partition depends on the magnitude of d: For d below 3, the change in discharge partition is more significant than for d larger than 3.

It seems reasonable that in the "shallow" flow scenarios (SS and RS), the bias induced by model geometric distortion is greater, since the effect of geometric distortion tends to shift the flow type from "shallow" to "deep." This effect is amplified when the flow is rapid (high Froude number) such as in the RS scenario. Overall, the bias resulting from model geometric distortion is doubled when the lumped Froude number F_0 is varied from 0.2 (Scenarios SS and SD) to 0.6 (Scenarios RS and RD).

A bias of the order of maximum 10%, as revealed by our simulations, is consistent with recent results obtained by Li et al. (2019), who reanalyzed experimental data of Finaud-Guyot et al. (2018). Indeed, they also found a bias of up to 10% induced by model distortion and the flooding scenario they considered was close to the "rapid shallow" scenario (RS) defined here, since the downstream boundary condition of Finaud-Guyot et al. (2018) was a free overflow. This is further detailed in Text S3 and Figure S9 in the supporting information.

4.2.2. Direction of the Bias Induced by Geometric Distortion

For the shallow flow scenarios (SS and RS), the overall tendency is a reduction of the upscaled flow depth as the distortion ratio is increased, at least for values of the distortion ratio d up to 10 to 15. This trend was

expected. Indeed, as discussed in section 2, it is consistent with an increase in the Reynolds number R_m and a decrease in the relative roughness $k_{s,m}/h_m$ as the distortion ratio rises, since these two effects tend to lower the friction coefficient computed based on Equation 6 and hence the frictional losses over the urban district. The trend of the discharge partition remains also monotonous for all distortion ratios up to $d \sim 15$.

The decreasing trend of $h*$ for Scenarios SS and RS strongly contrasts with the computed results for the deep flow scenarios (SD and RD). Indeed, in these cases, the upscaled flow depth decreases when the distortion ratio is varied between 1 and about 4–5; but surprisingly, it increases for higher values of d (Figure 4). Similarly, Figure 5 reveals a nonmonotonous pattern of the outflow discharge at Outlets 1 and 3, while the outflow discharge at Outlet 2 is less affected by distortion.

To clarify whether this nonmonotonous pattern of the upscaled flow depth and discharge partition is specific to the "deep" Scenarios SD and RD, or whether it can also be observed for the "shallow" Scenarios SS and RS, we extended the range of tested distortion ratios for Scenarios SS and RS (d up to 25). Although to a lesser extent than for Scenarios SD and RD, the computed results reveal a slight nonmonotonous behavior of the upscaled flow depth even for Scenarios SS and RS (Figure 4). Similarly, the portion of discharge obtained at Outlet 1 for $d = 25$ is slightly greater than for $d = 10$ (Scenario SS) or 16.67 (Scenario RS). At Outlet 3, the flow partition corresponding to $d = 25$ is slightly smaller than for $d = 10$ (Scenario SS) or 16.67 (Scenario RS). This suggests that, for all scenarios, a competition exists between the decline of the friction coefficient as d increases and another process which tends to amplify losses for increasing values of d. This is further discussed in section 5.

4.2.3. Influence of the Horizontal Scale Factor

The results presented in Figures 4 and 5 are all based on simulations conducted for $e_H = 50$. To appreciate the influence of e_H on our findings, computations were also performed for $e_H = 20$ and $e_H = 100$ for the Flooding Scenarios SS and RD.

The dependency of the computed upscaled flow depth and discharge partition on d remains very similar for the three horizontal scale factors, as shown in Figures S10 and S11 (supporting information). For example, for the "deep" flow scenario (RD), the minimum in the curve representing $h*$ as a function of d is located close to $d = 4$ for all three horizontal scale factors. For a given scenario, a significant vertical shift is observed between the values of $h*$ computed for different values of e_H. This highlights the presence of "scale" effects, regardless of whether the models are geometrically distorted or not.

Regarding the discharge partition, the bias induced by model distortion is systematically stronger when the horizontal scale factor is larger, as also demonstrated in Table S5 in the supporting information (e.g., almost 12 percentage points for $e_H = 100$ compared to 8 percentage points for $e_H = 20$ at Outlet 3 for Scenario SS).

4.3. Extent of Flow Separation Zones

We examine here the extent of the computed flow separation zones at two selected locations downstream of street intersections: "Zone A1" and "Zone B3" as highlighted by green boxes in Figure 2. We used the stream function to identify isocumulative flow discharge curves, which define the boundary of the flow separation zones (Tartinville et al., 1997). Figures S12 and S13 (in the supporting information) show the flow separation in Zones B3 and A1 for $e_H = 50$, for various distortion ratios and all four flooding scenarios.

The width and length of the separation zones, normalized by the street width, are noted W^* and L^*, respectively. Notations X^* and Y^* refer to the spatial coordinates x and y defined in Figure 2, normalized by the channel width b_m. As shown in Figures 6 and 7, the lengths and widths of the flow separation zones are larger in the case of "slow flow" scenarios (SS and SD) than in the "rapid flow" scenarios (RS and RD).

For the "slow" flow scenarios (SS and SD), the flow separation in Zone B3 remains virtually unchanged when the distortion ratio is varied, whereas the flow separation zones vary nonmonotonously for the "rapid" flow scenarios (Figure 6). They are initially reduced as d increases from 1 to 3–4 for RD scenarios, or from 1 to 12.5 for RS scenarios, and afterward they increase with increasing d. This appears consistent with the pattern of the outflow discharge at Outlet 3 when d is varied, as well as with the change in h^* with d (Figures 4 and 5).

In Zone A1, for the "shallow" flow scenarios (SS and RS), the flow separation zone expands for d up to 10 and shrinks slightly for higher values of d (Figure 7). This is again consistent with the pattern of the outflow discharge at Outlet 1 (Figure 5). The same applies for the "deep" flow scenarios (SD and RD); but in this case the
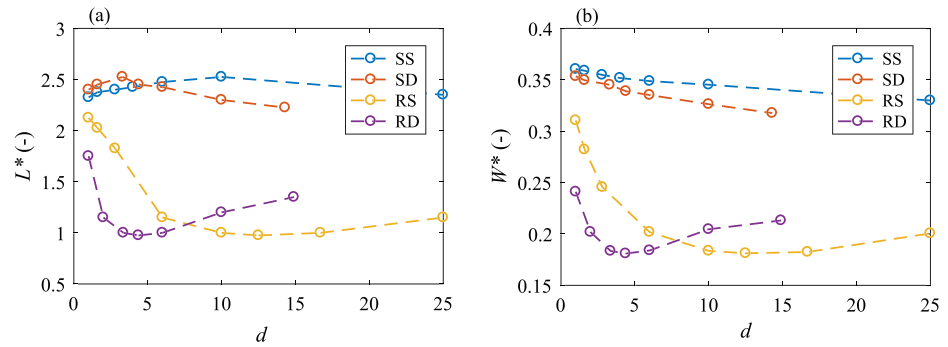
Figure 6. (a) Length L^* and (b) width W^* of separation zone (normalized by street width) for $e_H = 50$ in Zone B3 (as defined in Figure 2) and the four flooding scenarios.

separation zone keeps expanding only until d reaches a value of 3 to 4, instead of 10. These critical values of d (10 for the "shallow" scenarios and 3 to 4 for the "deep" scenarios) are remarkably consistent with those obtained for the changes in the direction of trends of the standardized flow depths (Figure 4) as well as of the outflow discharge partitions (Figure 5).

The separation zones obtained for the other horizontal scale factors ($e_H = 20$ and $e_H = 100$) are shown in Figure S14 and Figure S15 (in the supporting information) and reveal a very similar influence of the model geometric distortion on flow separation zones for all three horizontal scale factors.

Overall, the whole set of results reveals consistent trends between the evolution of (i) the inlet flow depth (Figure 4), (ii) the partition of outflow discharge (Figure 5), and (iii) the dimensions of the flow separation zones (Figures 6 and 7), when the model geometric distortion is varied.

5. Interpretation

In section 4, we suggested that a competition between the declining friction coefficient and another effect is responsible for the nonmonotonous relationship of the examined flow variables with the distortion ratio (Figures 4–7). To analyze this further, we have repeated some of the computations (i) without the effect of sidewall friction (section 5.1) and (ii) by replacing the network of streets with a prismatic channel, in order to isolate the friction effects (section 5.2). Next, we present a power balance analysis, to evaluate if a competition between frictional and local losses could explain the nonmonotonous relationship between the examined flow variables and the model geometric distortion (section 5.3).

5.1. Effect of Sidewall Friction

A first hypothesis we formulated was that the change in the aspect ratio h_m/b_m with d (section 2) would be responsible for the observed nonmonotonous behavior. Indeed, for a constant width, a greater aspect ratio
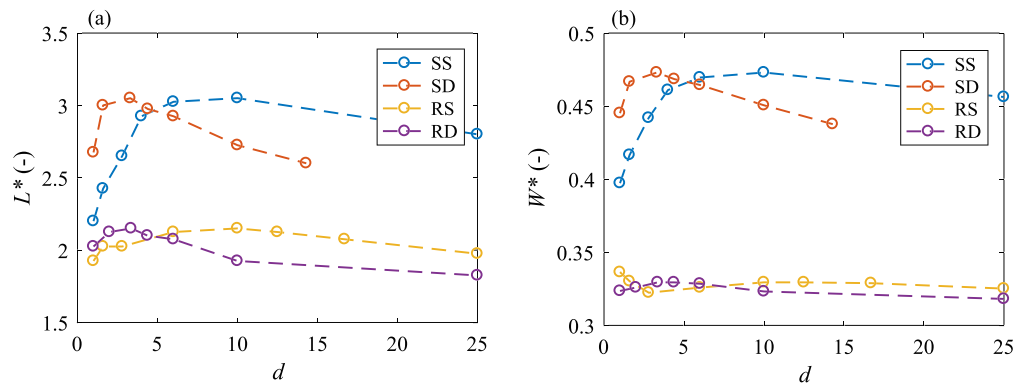

Figure 7. (a) Length L^* and (b) width W^* of separation zone (normalized by street width) for $e_H = 50$ in Zone A1 (as defined in Figure 2) and the four flooding scenarios.
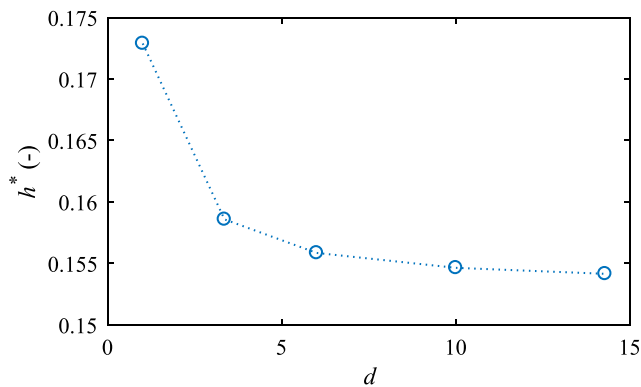
Figure 8. Standardized upscaled flow depth $h^* = h_m e_V/(b_m e_H)$ at the inlet (centerline) of a prismatic channel (same length and width as Street B3) as a function of the model geometric distortion, for a horizontal scale factor $e_H = 50$ and in Flooding Scenarios RD.

leads to a larger wetted perimeter due to higher water depths, which results in increased sidewall friction. We also hypothesized that this effect should be dominating in the case of the relatively deep flow scenarios (SD and RD). To test this hypothesis, we repeated the numerical simulations for two scenarios (SS and RD) by setting the computed sidewall friction to 0. The computational results suggest that the hypothesis is not correct. Indeed, as shown in Figures 4a and 4d, the values of upscaled flow depths computed without sidewall friction (labeled "B" in Figure 4) are indeed lower than those accounting for the sidewall friction (labeled "B + L" in Figure 4) since less frictional losses occur; but this difference does not cancel the nonmonotonous behavior.

Since none of the parameters controlling the frictional losses (R_m, $k_{s,m}/h_m$, and h_m/b_m) seems to explain the increase in the upscaled water depth for large distortion ratios, we hypothesize now that a competition with *local losses* (flow merging and separation at crossroads, hydraulic jumps, etc.) could be responsible for this result, as discussed hereafter (Luo et al., 2018).

5.2. Prismatic Channel

We consider here a prismatic channel with the same width and length as Street B3 (Figure 2). Since flow separation is not expected to occur in such a prismatic channel, we postulate that the head losses are dominated by frictional losses and not by local losses. This holds true in the framework of 2-D computational modeling, whereas in reality secondary currents may develop, particularly in relatively narrow channels. The computation was performed for $e_H = 50$ and Scenario RD, for which a marked nonmonotonous evolution of h^*, flow partition and dimensions of flow separation zones, was obtained in the case of the network of streets (Figures 4–7).

As shown in Figure 8, the standardized upscaled flow depth in the prismatic channel shows a perfectly monotonous decreasing trend as the distortion ratio is increased. The greater the model geometric distortion, the lower the computed upscaled flow depths, which is consistent with the analytical study of Li et al. (2019) based solely on frictional losses. Since these results contrast with the nonmonotonous variation obtained in Figure 4, they confirm the important influence of local losses on the effect of model geometric distortion in the case of a network of streets.

In quantitative terms, the difference shown in Figure 8 between distorted and undistorted models of the prismatic channel reaches up to 10%, which is much higher than the differences found for Scenario RD in the network of streets (Figure 4). This also hints at the role of another process than frictional losses, which competes with the effect of frictional losses and, in the case of the network of streets, ends up damping the bias resulting from model geometric distortion.

5.3. Power Balance

Combining/separating discharges, due to multiple inlets and outlets, does not allow using a head balance encompassing the whole district, in the form of a Bernoulli equation. Hence, here, we compute the difference between the power entering the flow domain and the power leaving the flow domain, that is, the total power dissipation across the urban district. Afterward, we link the loss mechanisms embedded in the numerical model to the corresponding portions of the total power loss.

As summarized in Table 3, the numerical model we used contains two types of terms, which lead to power dissipation (Camnasio et al., 2014; Erpicum et al., 2009). On one hand, the bed shear stress and, on the other hand, the terms resulting from the depth averaging of the Reynolds stresses. The former remains nonzero even in uniform flow conditions. As such it is closely related to vertical shear in the flow and so to frictional losses due to the bottom. Frictional losses due to lateral walls generate shear in other directions, but they are included in the same term,

Table 3
Terms Modeling Losses in the 2-D Numerical Model

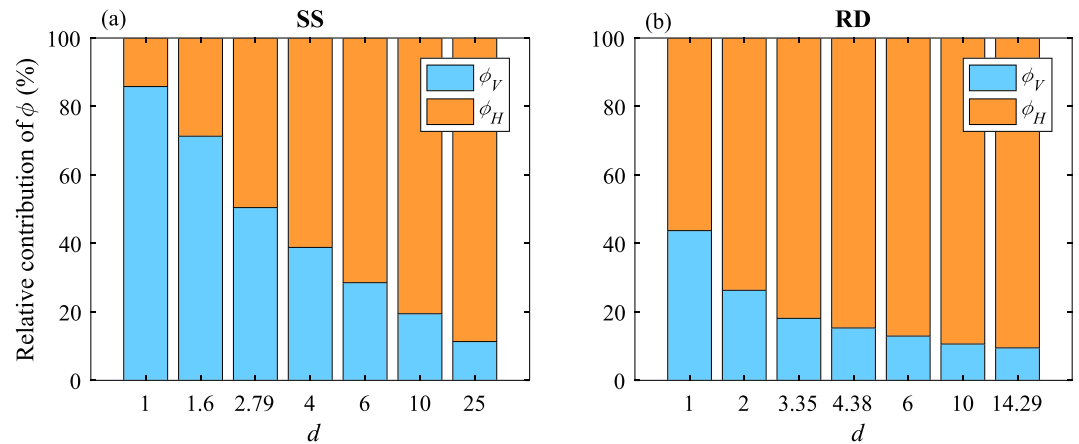|	Bed shear stress	Depth-averaged effect of Reynolds stresses
Under uniform flow conditions	Nonzero	Zero
Closely related to losses induced by	Vertical shear	Horizontal shear
Label in Equations S1 and S2 in Text S1	①	②

Figure 9. Relative contribution of ϕ_V ("vertical shear") and ϕ_H ("horizontal shear") to the total power dissipation as a function of the distortion ratio d, for Scenarios (a) SS and (b) RD and the horizontal scale factor $e_H = 50$.

through their contribution to the wetted perimeter. The second term involves horizontal gradients of the flow variables, and therefore, it vanishes in the case of uniform flow conditions. We relate these terms mostly to the effects of horizontal shear, which is particularly strong in the case of local head losses such as flow separation.

In the following, we distinguish between these two contributions to the total dissipated power by referring to "losses induced by vertical shear" (noted ϕ_V) and "losses induced by horizontal shear" (noted ϕ_H). The mathematical and numerical formulations used to quantify these two contributions are detailed in Text S4 in the supporting information.

Figure 9 presents the relative contributions of vertical shear (ϕ_V) and horizontal shear (ϕ_H) to power dissipation, as a function of the distortion ratio d, for $e_H = 50$ and for scenarios SS and RD. The following observations can be made:

1. The relative importance of ϕ_V and ϕ_H is found to strongly depend on the considered scenario. In the undistorted case, the computed contribution of ϕ_V to power dissipation exceeds 85% for Scenario SS ("shallow" flow), while it does not even reach 50% in Scenario RD ("deep" flow).
2. For both scenarios, the relative importance of ϕ_V becomes less prominent as the distortion ratio is increased, whereas the relative importance of ϕ_H grows. This result is consistent with our hypothesis that the relative importance of frictional losses (linked mostly to vertical shear) decreases when a scale model gets more distorted; while the relative importance of local losses (closely linked to horizontal shear) is magnified.

The relative importance of ϕ_V and ϕ_H varies similarly with d whatever the horizontal scale factors ($e_H = 20$, 50 or 100), as shown in Figures S18 and S19 (in the supporting information). Nonetheless, Figure S19 also reveals that the contribution of ϕ_V is systematically higher for smaller scale models (i.e., higher value of e_H), which is consistent with well-established knowledge on scale effects: the smaller the scale model, the higher the relative importance of boundary effects such as friction (Heller, 2011).

Figure 10 presents the total power dissipation scaled by the inlet power, as a function of d for $e_H = 50$ and for the four flooding scenarios. It reveals that the competition between ϕ_H and ϕ_V as highlighted in Figure 9 results in a nonmonotonous variation of the total dissipation when the distortion ratio is varied, particularly in the "deep" flow scenarios (SD and RD). This result appears perfectly consistent with those obtained for the computed upscaled flow depths (Figure 4), discharge partition (Figure 5), and size of recirculation zones (Figures 6 and 7). Even in quantitative terms, the agreement between the variations of total power dissipation and upstream flow depths with d is very good (Table 4), which is not surprising since for low Froude numbers the gradient in flow depth tends to be a reasonable proxy for energy slope. The minimum values of h^* and of the total power dissipation are obtained for fairly the same values of d. Similar trends are
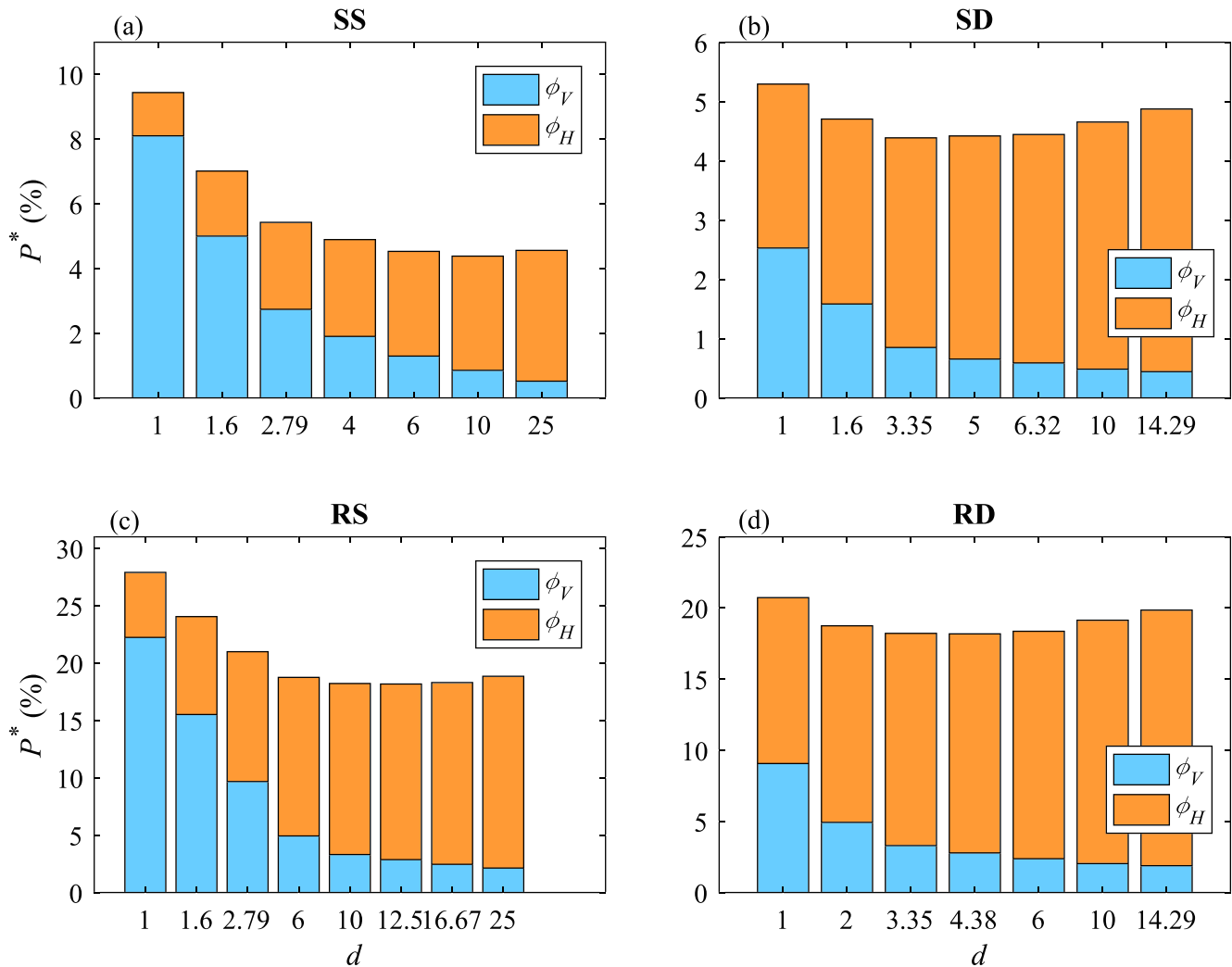
Figure 10. Relative power dissipation $P^* = (P_{in} - P_{out})/P_{in}$ for $e_H = 50$ in the (a–d) four flooding scenarios.

obtained for $e_H = 20$ and $e_H = 100$ (Figure S20 in the supporting information). Note that in general the effect of changing the horizontal scale factor is reduced when the distortion ratio is increased.

Another hint of the role of horizontal shear in explaining the nonmonotonous results is obtained by examining the power balance in the case of a prismatic channel, as in section 5.2. As shown in Figure S21 (supporting information), a monotonous trend is observed for this case, since the horizontal shear is expected to be very low compared to the case with intersections.

Table 4
Maximum Effect of Model Distortion on Flow Depth and Power Dissipation: $\Delta h^* = \left[h^*\big|_{d=1} - \min_{d}\left(h^*\right)\right]/h^*\big|_{d=1}$ *and*

$\Delta P = P^*\big|_{d=1} - \min_{d}\left(P^*\right)$

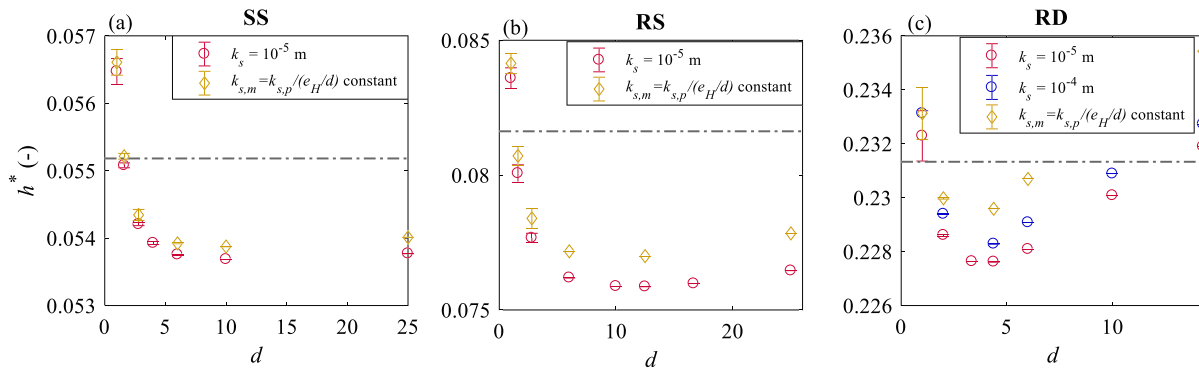|	Scenario SS		Scenario RD		Scenario RS		Scenario RD	
	Δh^* (%)	ΔP (%)	Δh^* (%)	ΔP (%)	Δh^* (%)	ΔP (%)	Δh^* (%)	ΔP (%)
$e_H = 20$	3.6	3.73	1.3	1.93	—	—	—	—
$e_H = 50$	5.2	5.1	2.1	2.55	10.2	9.73	0.89	0.9
$e_H = 100$	6.9	7.9	2.5	3	—	—	—	—

Figure 11. Upscaled normalized flow depths for $e_H = 50$ and (a–c) various flooding scenarios considering either a fixed roughness height $k_{s,m} = 10^{-5}$ m or a fixed relative roughness: $k_{s,m} = k_{s,p}/(e_H/d)$. The horizontal dash-dotted line represents the results at prototype scale assuming $k_{s,p} = 0.005$ m.

However, it is of utmost importance to stress that all results presented here were obtained with a depth-averaged 2-D computational model. This type of model may lead to issues with representation of recirculations and form drag, particularly when the distortion increases (deeper flow, for which the shallow-water assumptions are less valid). Therefore, additional analyses based on accurate 3-D computational modeling or laboratory experiments are needed to clarify whether the present findings reflect the actual flow physics or whether they merely result from an artifact of the 2-D model, as discussed in section 6.2.

6. Discussion

6.1. Influence of Roughness Height

Urban areas are very heterogeneous, which makes it challenging to identify a representative value of roughness height. Therefore, we postulate here a plausible value of $k_{s,p} = 0.005$ m, which seems reasonable to characterize the surface of standard materials encountered in urban environments such as asphalt or pavements. We also test alternate values of roughness height, namely $k_{s,p} = 0.01$ m and $k_{s,p} = 0.05$ m, which may lump the effect of small-scale obstacles such as sidewalks (Figures S22 and S23 in the supporting information).

In all simulations so far, we considered a roughness height $k_{s,m} = 10^{-5}$ m for the bottom and sidewalls of the scale models. This is indeed representative of standard material used for physical models in hydraulic laboratories (e.g., Plexiglas, PVC, and glass). However, according to Equation 4, this leads in general to a different relative roughness in the scale model compared to the prototype one, since $k_{s,m} \neq k_{s,p}/(e_H/d)$. An alternate approach consists in selecting, for each distortion value, a specific material for the scale model so that the roughness height corresponds to the prototype roughness height divided by the vertical scale factor: $k_{s,m} = k_{s,p}/(e_H/d)$. This enables preserving the same relative roughness at prototype scale and in the scale model, at the expense of having to change the scale model material if the distortion ratio is varied (since $k_{s,m}$ depends on d).

Hence, assuming a prototype-scale roughness height $k_{s,p}$ of 0.005 m and a horizontal scale factor $e_H = 50$, the corresponding roughness height in the scale model ranges between 10^{-4} m and 25×10^{-4} m for distortion ratios d ranging from 1 to 25.

Figure 11 compares the computed flow depths obtained by considering either a fixed roughness height $k_{s,m} = 10^{-5}$ m in the scale model or the same relative roughness as in the prototype: $k_{s,m} = k_{s,p}/(e_H/d)$. The differences in the results remain in general relatively small. In Scenarios SS and RS, the differences are below 0.25% for undistorted models and they grow up to 1.8% for the most distorted cases. This indicates that the bias induced by model distortion is generally larger than the effect of changing the scale model material. For Scenario RD, the effect of changing the roughness remains small compared to the values of h^*, but in this case, the effect is of the same order as the influence of the distortion.

For Scenario RD, we also tested a fixed roughness height $k_{s,m} = 10^{-4}$ m, selected so that in the undistorted model the relative roughness agrees with that of the prototype-scale. The differences remain very limited as shown in Figure 11c.

In Figure 11, we also display the dimensionless flow depths obtained from simulations at the prototype scale, considering $k_{s,p} = 0.005$ m (horizontal dash-dotted line). It appears that the best agreement is not obtained for $d = 1$, even when the relative roughness is set to the same value as at prototype scale. This results from the considerable reduction in Reynolds number in the undistorted scale model compared to the prototype scale. Another remarkable result is that two distinct distortion ratios ($d \sim 1.5$ and 12) lead to a good agreement with the prototype-scale result for Scenario RD. This is discussed further in section 6.2.

6.2. Validity of 2-D Modeling

Depth-averaged 2-D computational models have proved valid in many instances, but limitations in their validity remain when it comes to predicting flows significantly influenced by form drag and recirculations. Table S6 in the supporting information presents a selection of studies, which assessed the ability of 2-D models to deliver accurate predictions of various flow variables in configurations similar to those encountered in urban flooding: flow in a synthetic urban district (Arrault et al., 2016), as well as subcritical flow divisions (Bazin et al., 2017; Bruwier et al., 2017; Khan et al., 2000; Shettar & Murthy, 1996) and junctions in 90° sharp-edged rectangular open channels of equal width (El Kadi Abderrezzak & Paquier, 2009; Khan et al., 2000).

In all cases detailed in Table S6, the 2-D model delivered accurate predictions for at least the flow discharge partition and the water surface profiles. Moreover, the computation of these two quantities remains generally insensitive to the particular turbulence model used (e.g., constant eddy viscosity and k-ε model).

In the case of flow in an urban district, only the flow discharge partition and the water depths were used for evaluating the 2-D model (Arrault et al., 2016). In contrast, for some of the more generic configurations of flow divisions and junctions, the performance of the 2-D model was also analyzed in terms of extent of computed recirculation cells and velocity fields. While Bazin et al. (2017), Shettar and Murthy (1996), and Khan et al. (2000) all report a fair to good agreement between computed and observed velocity profiles, only Shettar and Murthy (1996) state that the computed length and width of recirculation cells showed an "acceptable" agreement with the observations. Contrarily, Bazin et al. (2017) highlight that the 2-D model failed to predict accurately the extent of the flow recirculations. Several studies emphasize the sensitivity of the computed recirculation widths and lengths to the particular parametrization used for turbulence closure (Arrault et al., 2016; Bazin et al., 2017; Bruwier et al., 2017).

These results suggest that, although depth-averaged 2-D computational models have been very successful in predicting flow depths, discharge partition, and, to some extent, velocity profiles, in configurations similar to that of interest here, their ability to accurately predict the extent of recirculation cells and, hence, the overall effect of form drag and local head losses, as well as their relative importance, may still be questioned. This highlights the need for complementing the present study based on nonhydrostatic 3-D computational modeling and dedicated laboratory experiments.

6.3. Design of Scale Models of Urban Flooding

In the previous sections, we extensively discussed the possible bias induced by model geometric distortion. In practice, this effect is combined with measurement uncertainties. To address this, we introduce Figure 12, which presents essentially the same results as in Figure 4, but two additional pieces of information are provided. First, the results obtained from simulations at prototype scale (assuming $k_{s,p} = 0.005$ m) are also displayed, like in Figure 11. Second, the error bars in Figure 12 reflect the uncertainty affecting the measured upscaled flow depths (i.e., the predictions made from the laboratory experiments) when a fixed measurement uncertainty is assumed in the scale models. The magnitude of this measurement uncertainty was set here to a plausible value of 1 mm.

If we initially disregard the effect of measurement uncertainties (i.e., the error bars in Figure 12), it appears that for a given prototype-scale flooding scenario and roughness height, the potential bias induced by model geometric distortion may be reduced to zero by a proper selection of d. Depending on the scenario, either a single "optimal" value of d (Scenarios SS and RS) or two distinct "optimal" values of d (Scenarios SD and RD) lead to a perfect agreement between the prototype-scale result and the values obtained for a reduced scale.
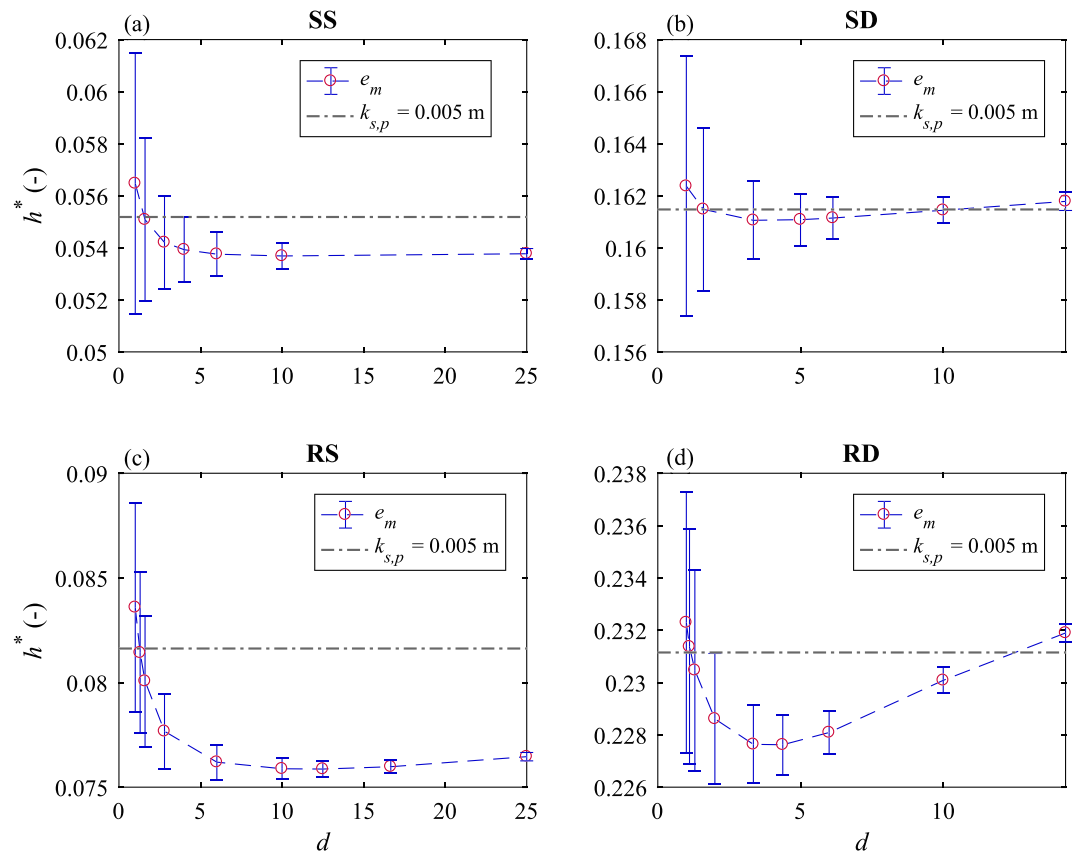
Figure 12. Standardized upscaled flow depth h^* at Inlet A as a function of the model geometric distortion, for a horizontal scale factor $e_H = 50$ and in the (a–d) four considered flooding scenarios. Error bars represent the effect of an assumed 1-mm measurement uncertainty in the scale models.

For all flooding scenarios, one "optimal" value of d is close (but not equal) to unity, while the second one is considerably larger (above 10) when it exists.

In the cases where two "optimal" values of d appear, Figure 12 suggests that the larger one should be chosen as it enables a considerable reduction in the effect of measurement uncertainties on the upscaled values. However, from another perspective, this choice seems unacceptable. Indeed, in Figures 9 and 10, we showed that for relatively high distortion ratios (above 10), the losses related to horizontal shear dominate power dissipation. This contrasts with the results obtained at prototype scale (Figures S18 and S24 in the supporting information), for which the vertical shear contributes much more to the total power dissipation. In other words, although a good match between the upscaled scale-model and prototype-scale results match for d close to or above 10 in Scenarios SD and RD, it does so for "wrong reasons"; that is, the main underlying dissipation mechanism is not the correct one in the scale model compared to the prototype case.

However, simply picking the smaller value of d which minimizes the distortion-induced bias is also not a viable option since the influence of measurement uncertainties would be unacceptably high for many real-world applications. To sum up, no "perfect" distortion ratio seems available, and a trade-off must be sought between measurement precision and representativeness of flow processes.

As a consequence, we suggest the following approach to scale urban flooding in a network of streets:

1. from the specific objectives of the study, determine the minimum precision required on the predictions;
2. select the smallest possible value of d which enables keeping the effect of measurement uncertainties below the targeted precision (Figure 12);

3. use the results of this study (or tailored numerical simulations) to estimate the direction and magnitude of the bias induced by the selected distortion ratio and, if relevant, compensate the upscaled values.

In general, it is not worth the effort to change the scale model material ($k_{s,m}$), as demonstrated in Figure 11.

7. Conclusions

Based on 2-D computational modeling, this paper presents a systematic study of the effects of model geometric distortion in the case of laboratory experiments of urban flooding in a network of streets. We defined four types of flooding scenarios, characterized by contrasting flow depths ("shallow" vs. "deep") and lumped Froude numbers ("slow" vs. "rapid" flow). For a synthetic urban layout, we performed numerical simulations based on reduced-scale geometries (mimicking laboratory scale models) and for the prototype-scale geometry (used as a reference). For the former, we analyzed the results upscaled to the prototype scale, that is, the predictions from the simulated scale models.

We found a generally weak effect of the model geometric distortion on the upscaled flow variables. The magnitude of the effect differs substantially between the considered flooding scenarios. For the relatively "deep" flow, the influence of model geometric distortion on the upscaled flow depths at the inlets is of the order of 1% to 2%. In contrast, these differences rise up to 5% to 10% for the relatively "shallow" flooding scenarios. In general, the influence of model geometric distortion is doubled when the lumped Froude number increases from 0.2 ("slow" flow scenario) to 0.6 ("rapid" flow scenario). In the "deep" flow scenarios, like the upstream flow depths, the discharge partition at the outlets is only slightly influenced (1 to 2 percentage points) by a change in the distortion ratio. In contrast, discharge partitions in the "shallow" flow scenarios are more influenced by distortion (of the order of 5 to 10 percentage points), which is again similar to the effect of distortion on the flow depths. Overall, the simulation results indicate that the influence of model geometric distortion is generally stronger than the effect of changing the roughness, that is, the scale model material.

In the "shallow" flow scenarios, the direction of change of the upscaled flow depths when the distortion ratio is increased is mostly a monotonous decrease (in the range of d of practical relevance), due to a decrease in frictional losses. This result contrasts with those obtained for the "deep" flow scenarios, which show a nonmonotonous evolution when the distortion is varied. Based on the analysis of power dissipation, we attribute this nonmonotonous evolution to a competition between declining frictional losses and increasing local losses. For the same flooding scenarios, the discharge partition and size of the flow separation zones show a similar nonmonotonous pattern, with the extrema located at approximately the same value of distortion for all flow variables.

Although the computational model used here showed excellent performance to predict water profiles and flow discharge in previous studies, it becomes in principle less valid for high distortion ratios (as the shallow-water assumptions become less valid). Therefore, at this stage, we cannot eliminate the possibility that some of our findings result from an artifact of 2-D depth-averaged flow modeling. To sort this out, the only two options are to perform computations with a validated 3-D numerical model (Luo et al., 2018) or to conduct dedicated laboratory experiments. The results presented here synthetize "the best that a 2-D flow model can teach us" about the effect of model geometric distortion for the case of urban flooding in a small synthetic district.

In practice, a trade-off must be sought between (i) precision of the predictions issued from a scale model and (ii) preservation of a turbulent flow regime (both advocating for high distortion ratios) and representativeness of the different dissipation mechanisms in the flow (advocating for relatively low distortion ratios). The merit of the present study is to provide quantitative insights into the bias induced by the selection of a specific distortion ratio (Figure 12).

Also, we investigated here the influence of model geometric distortion for a simplified configuration (limited number of straight streets intersecting at 90°). Further analysis is required regarding the influence of model geometric distortion on additional processes such as the effect of a steeper bottom slope, more complex urban forms, the presence of obstacles such as urban furniture, and flow exchanges with urban drainage systems.

Data Availability Statement

Data sets for this research are available online (https://doi.org/10.5281/zenodo.3739167).

References

Arndt, R., Roberts, P., & Wahl, T. (2000). In R. Ettema (Ed.), *Hydraulic modeling: Concepts and practice.* American Society of Civil Engineers.

Arrault, A., Finaud-Guyot, P., Archambeau, P., Bruwier, M., Erpicum, S., Pirotton, M., & Dewals, B. (2016). Hydrodynamics of long-duration urban floods: Experiments and numerical modelling. *Natural Hazards and Earth System Sciences*, *16*(6), 1413–1429. https://doi.org/10.5194/nhess-16-1413-2016

Arrighi, C., Oumeraci, H., Castelli, F. (2017). Hydrodynamics of pedestrians instability in floodwaters. *Hydrology and Earth System Sciences*, *21*(1), 515–531. https://doi.org/10.5194/hess-21-515-2017

Bazin, P.-H., Mignot, E., & Paquier, A. (2017). Computing flooding of crossroads with obstacles using a 2D numerical model. *Journal of Hydraulic Research*, *55*(1), 72–84. https://doi.org/10.1080/00221686.2016.1217947

Beven, K. (2006). A manifesto for the equifinality thesis. *Journal of hydrology*, *320*(1–2), 18–36. https://doi.org/10.1016/j.jhydrol

Brown, R., & Chanson, H. (2012). Suspended sediment properties and suspended sediment flux estimates in an inundated urban environment during a major flood event. *Water Resources Research*, *48*, W11523. https://doi.org/10.1029/2012WR012381

Brown, R., & Chanson, H. (2013). Turbulence and suspended sediment measurements in an urban environment during the Brisbane River flood of January 2011. *Journal of Hydraulic Engineering*, *139*(2), 244–253. https://doi.org/10.1061/(ASCE)HY.1943-7900.0000666

Bruwier, M., Erpicum, S., Archambeau, P., Pirotton, M., & Dewals, B. (2017). Computing flooding of crossroads with obstacles using a 2D numerical model. *Journal of Hydraulic Research*, *55*(5), 737–741. https://doi.org/10.1080/00221686.2017.1326406

Camnasio, E., Erpicum, S., Archambeau, P., Pirotton, M., & Dewals, B. (2014). Prediction of mean and turbulent kinetic energy in rectangular shallow reservoirs. *Engineering Applications of Computational Fluid Mechanics*, *8*(4), 586–597. https://doi.org/10.1080/19942060.2014.11083309

Chanson, H. (1999). *The hydraulics of open channel flow: An introduction* (1st ed., p. 512). London, UK: Edward Arnold.

Chanson, H. (2004). Physical modelling of hydraulics. In H. Chanson (Ed.), *Hydraulics of open channel flow* (2nd ed., pp. 253–274). Oxford: Butterworth-Heinemann.

Chen, Y., Zhou, H., Zhang, H., Du, G., & Zhou, J. (2015). Urban flood risk warning under rapid urbanization. *Environmental Research*, *139*, 3–10. https://doi.org/10.1016/j.envres.2015.02.028

Chu, V. H., & Babarutsi, S. (1988). Confinement and bed-friction effects in shallow turbulent mixing layers. *Journal of Hydraulic Engineering*, *114*(10), 1257–1274. https://doi.org/10.1061/(ASCE)0733-9429(1988)114:10(1257)

Creëlle, S., Engelen, L., Schindfessel, L., Cunha Ramos, P. & De Mulder, T. (2018). Experimental investigation of free surface gradients in a 90° angled asymmetrical open channel confluence. In P. Gourbesville, J. Cunge, & G. Caignaert (Eds.), *Advances in Hydroinformatics* (pp. 803–819). Singapore: Springer.

Di Baldassarre, G., Kreibich, H., Vorogushyn, S., Aerts, J., Arnbjerg-Nielsen, K., Barendrecht, M., et al. (2018). Hess opinions: An interdisciplinary research agenda to explore the unintended consequences of structural flood protection. *Hydrology and Earth System Sciences*, *22*(11), 5629–5637. https://doi.org/10.5194/hess-22-5629-2018

El Kadi Abderrezzak, K., & Paquier, A. (2009). Discussion of numerical and experimental study of dividing open-channel flows. *Journal of Hydraulic Engineering*, *135*(12), 1111–1112.

Erpicum, S., Dewals, B. J., Archambeau, P., & Pirotton, M. (2010). Dam break flow computation based on an efficient flux vector splitting. *Journal of Computational and Applied Mathematics*, *234*(7), 2143–2151. https://doi.org/10.1016/j.cam.2009.08.110

Erpicum, S., Meile, T., Dewals, B. J., Pirotton, M., & Schleiss, A. J. (2009). 2D numerical flow modeling in a macro-rough channel. *International Journal for Numerical Methods in Fluids*, *61*(11), 1227–1246. https://doi.org/10.1002/fld.2002

Finaud-Guyot, P., Garambois, P.-A., Araud, Q., Lawniczak, F., François, P., Vazquez, J., & Mosé, R. (2018). Experimental insight for flood flow repartition in urban areas. *Urban Water Journal*, *15*(3), 242–250. https://doi.org/10.1080/1573062X.2018.1433861

Fraga, I., Cea, L., & Puertas, J. (2017). Validation of a 1D-2D dual drainage model under unsteady part-full and surcharged sewer conditions. *Urban Water Journal*, *14*(1), 74–84. https://doi.org/10.1080/1573062X.2015.1057180

Güney, M. S., Tayfur, G., Bombar, G., & Elci, S. (2014). Distorted physical model to study sudden partial dam break flows in an urban area. *Journal of Hydraulic Engineering*, *140*(11), 05014006. https://doi.org/10.1061/(ASCE)HY.1943-7900.0000926

Heller, V. (2011). Scale effects in physical hydraulic engineering models. *Journal of Hydraulic Research*, *49*(3), 293–306. https://doi.org/10.1080/00221686.2011.578914

Henderson, F. M. (1966). *Open channel flow.* New York, USA: MacMillan Company.

Hettiarachchi, S., Wasko, C., & Sharma, A. (2018). Increase in flood risk resulting from climate change in a developed urban watershed— The role of storm temporal patterns. *Hydrology and Earth System Sciences*, *22*(3), 2041–2056. https://doi.org/10.5194/hess-22-2041-2018

Ishigaki, T., Keiichi, T. & Kazuya, I. (2003). Hydraulic model tests of inundation in urban area with underground space. *Proc. of XXX IAHR Cogress* (pp. 487–493). Greece. Available from https://ci.nii.ac.jp/naid/10029665177/en/

Jongman, B. (2018). Effective adaption to rising flood risk. *Nature communication*, *9*(1986). https://doi.org/10.1038/s41467-018-04396-1

Jung, S., Kang, J., Hong, I., & Yeo, H. (2012). Case study: Hydraulic model experiment to analyze the hydraulic features for installing floating islands. *Scientific Research*, *4*, 90–99. https://doi.org/10.4236/eng.2012.42012

Khan, A. A., Cadavid, R., & Wang, S. S. Y. (2000). Simulation of channel confluence and bifurcation using the CCHE2D model. *Proceedings of the Institution of Civil Engineers-Water Maritime and Energy*, *142*(2), 97–102. https://doi.org/10.1680/wame.2000.142.2.97

LaRocque, L. A., Elkholy, M., Chaudhry, M. H., & Imran, J. (2013). Experiments on urban flooding caused by a levee breach. *Journal of Hydraulic Engineering*, *139*(9), 960–973. https://doi.org/10.1061/(ASCE)HY.1943-7900.0000754

Leitão, J. P., Peña-Haro, S., Lüthi, B., Scheidegger, A., & Moy de Vitry, M. (2018). Urban overland runoff velocity measurement with consumer-grade surveillance cameras and surface structure image velocimetry. *Journal of Hydrology*, *565*, 791–804. https://doi.org/10.1016/j.jhydrol.2018.09.001

Li, X., Erpicum, S., Bruwier, M., Mignot, E., Finaud-Guyot, P., Archambeau, P., et al. (2019). Technical note: Laboratory modelling of urban flooding: Strengths and challenges of distorted scale models. *Hydrology and Earth System Sciences*, *23*(3), 1567–1580. https://doi.org/10.5194/hess-23-1567-2019

Lipeme Kouyi, G., Rivière, N., Vidalat, V., Becquet, A., Chocat, B., & Guinot, V. (2010). Urban flooding: One-dimensional modelling of the distribution of the discharges through cross-road intersections accounting for energy losses. *Water Science and Technology*, *61*(8), 2021–2026. https://doi.org/10.2166/wst.2010.133

Liu, H., Wang, Y., Zhang, C., Chen, A. S., & Fu, G. (2018). Assessing real options in urban surface water flood risk management under climate change. *Natural Hazards*, *94*(1), 1–18. https://doi.org/10.1007/s11069-018-3349-1

Lopes, P., Carvalho, R. F., & Leandro, J. (2017). Numerical and experimental study of the fundamental flow characteristics of a 3D gully box under drainage. *Water Science and Technology*, *75*(9), 2204–2215. https://doi.org/10.2166/wst.2017.071

Luo, H., Fytanidis, D. K., Schmidt, A. R., & Garcia, M. H. (2018). Comparative 1D and 3D numerical investigation of open-channel junction flows and energy losses. *Advances in Water Resources*, *117*, 120–139. https://doi.org/10.1016/j.advwatres.2018.05.012

Macchione, F., Costabile, P., Costanzo, C., & De Lorenzo, G. (2019). Extracting quantitative data from non-conventional information for the hydraulic reconstruction of past urban flood events. A case study. *Journal of Hydrology*, *576*, 443–465. https://doi.org/10.1016/j.jhydrol.2019.06.031

Martins, R., Kesserwani, G., Rubinato, M., Lee, S., Leandro, J., Djordjevic, S., & Shucksmith, J. D. (2017). Validation of 2D shock capturing flood models around a surcharging manhole. *Urban Water Journal*, *14*(9), 892–899. https://doi.org/10.1080/1573062X.2017.1279193

McCabe, M. F., Rodell, M., Alsdorf, D. E., Miralles, D. G., Uijlenhoet, R., Wagner, W., et al. (2017). The future of Earth observation in hydrology. *Hydrology and Earth System Sciences*, *21*(7), 3879–3914. https://doi.org/10.5194/hess-21-3879-2017

Mignot, E., Li, X., & Dewals, B. (2019). Experimental modelling of urban flooding: A review. *Journal of Hydrology*, *568*, 334–342. https://doi.org/10.1016/j.jhydrol.2018.11.001

Mignot, E., Paquier, A., & Haider, S. (2006). Modeling floods in a dense urban area using 2D shallow water equations. *Journal of Hydrology*, *327*(1–2), 186–199. https://doi.org/10.1016/j.jhydrol.2005.11.026

Mignot, E., Zeng, C., Dominguez, G., Li, C.-W., Rivière, N., & Bazin, P.-H. (2013). Impact of topographic obstacles on the discharge distribution in open-channel bifurcations. *Journal of Hydrology*, *494*, 10–19. https://doi.org/10.1016/j.jhydrol.2013.04.023

Molinari, D., & Scorzini, A. R. (2017). On the influence of input data quality to flood damage estimation: The performance of the INSYDE model. *Water*, *9*(9), 688. https://doi.org/10.3390/w9090688

Moy de Vitry, M., Dicht, S., & Leitão, J. P. (2017). floodX: urban flash flood experiments monitored with conventional and alternative sensors. *Earth System Science Data*, *9*(2), 657–666. https://doi.org/10.5194/essd-9-657-2017

Muste, M., Fujita, I., & Hauet, A. (2008). Large-scale particle image velocimetry for measurements in riverine environments. *Water Resources Research*, *44*, W00D19. https://doi.org/10.1029/2008WR006950

National Academies of Sciences Engineering and Medicine (2019). *Framing the challenge of urban flooding in the United States*. Washington, DC: The National Academies Press.

Novak, P., Guinot, V., Jeffrey, A., & Reeve, D. E. (2010). *Hydraulic modelling—An introduction* (p. 599). Taylor & Francis, London, UK: CRC Press. https://doi.org/10.1201/9781315272498

Perks, M. T., Russell, A. J., & Large, A. R. G. (2016). Technical note: Advances in flash flood monitoring using unmanned aerial vehicles (UAVs). *Hydrology and Earth System Sciences*, *20*(10), 4005–4015. https://doi.org/10.5194/hess-20-4005-2016

Pfister, M., & Chanson, H. (2012). Scale effects in physical hydraulic engineering models. Discussion. *Journal of Hydraulic Research, IAHR*, *50*(2), 244–246. https://doi.org/10.1080/00221686.2012.654672

Ramos, P. X., Schindfessel, L., Pêgo, J. P., & De Mulder, T. (2019). Flat vs. curved rigid-lid LES computations of an open-channel confluence. *Journal of Hydroinformatics*, *21*(2), 318–334. https://doi.org/10.2166/hydro.2019.109

Rivière, N., Travin, G., & Perkins, R. J. (2011). Subcritical open channel flows in four branch intersections. *Water Resources Research*, *47*, W10517. https://doi.org/10.1029/2011WR010504

Rivière, N., Travin, G., & Perkins, R. J. (2014). Transcritical flows in three and four branch open-channel intersections. *Journal of Hydraulic Engineering*, *140*(4), 04014003. https://doi.org/10.1061/(ASCE)HY.1943-7900.0000835

Rubinato, M., Martins, R., Kesserwani, G., Leandro, J., Djordjevic, S., & Shucksmith, J. (2017). Experimental calibration and validation of sewer/surface flow exchange equations in steady and unsteady flow conditions. *Journal of Hydrology*, *552*, 421–432. https://doi.org/10.1016/j.jhydrol.2017.06.024

Sharp, J. J., & Khader, M. H. A. (1984). Scale effects in harbour models involving permeable rubble mound structures. In H. Kobus (Ed.), *Symposium on scale effects in modelling hydraulic structures*. 2nd (pp. 7.12-1–7.12-5). Stuttgart, Germany: Technische Akademie Esslingen.

Shettar, A. S., & Murthy, K. K. (1996). A numerical study of division of flow in open channels. *Journal of Hydraulic Research*, *47*(5), 585–597. https://doi.org/10.3826/jhr.2009.3586

Smith, G. P., Rahman, P. F., & Wasko, C. (2016). A comprehensive urban floodplain dataset for model benchmarking. *International Journal of River Basin Management*, *14*(3), 345–356. https://doi.org/10.1080/15715124.2016.1193510

Sturm, M., Gems, B., Keller, F., Mazzorana, B., Fuchs, S., Papathoma-Köhle, M., & Aufleger, M. (2018). Experimental analyses of impact forces on buildings exposed to fluvial hazards. *Journal of Hydrology*, *565*, 1–13. https://doi.org/10.1016/j.jhydrol.2018.07.070

Tartinville, B., Deleersnijder, E., & Rancher, J. (1997). The water residence time in the Mururoa atoll lagoon: Sensitivity analysis of a three-dimensional model. *Coral Reefs*, *16*(3), 193–203. https://doi.org/10.1007/s003380050074

Teng, J., Jakeman, A. J., Vaze, J., Croke, B. F. W., Dutta, D., & Kim, S. (2017). Flood inundation modelling: A review of methods, recent advances and uncertainty analysis. *Environmental Modelling & Software*, *90*, 201–216. https://doi.org/10.1016/j.envsoft.2017.01.006

Testa, G., Zuccala, D., Alcrudo, F., Mulet, J., & Soares-Frazão, S. (2007). Flash flood flow experiment in a simplified urban district. *Journal of Hydraulic Research*, *45*, 37–44, [online] Available from: https://www.scopus.com/inward/record.uri?eid=2-s2.0-34247270217&partnerID=40&md5=6f5243924139c48c989752ae43d65f93

Velickovic, M., Zech, Y., & Soares-Frazão, S. (2017). Steady-flow experiments in urban areas and anisotropic porosity model. *Journal of Hydraulic Research*, *55*(1), 85–100. https://doi.org/10.1080/00221686.2016.1238013

Wakhlu, O. N. (1984). Scale effects in hydraulic model studies. In H. Kobus (Ed.), *Symposium on scale effects in modelling hydraulic structures* (2nd ed., 2.13-1–2.13-6). Stuttgart, Germany: Technische Akademie Esslingen.

Wang, R.-Q., Mao, H., Wang, Y., Rae, C., & Shaw, W. (2018). Hyper-resolution monitoring of urban flooding with social media and crowdsourcing data. *Computers & Geosciences*, *111*, 139–147. https://doi.org/10.1016/j.cageo.2017.11.008

Xia, J., Falconer, R. A., Wang, Y., & Xiao, X. (2014). New criterion for the stability of a human body in floodwaters. *Journal of Hydraulic Research*, *52*(1), 93–104. https://doi.org/10.1080/00221686.2013.875073

Yu, D., Yin, J., & Liu, M. (2016). Validating city-scale surface water flood modelling using crowd-sourced data. *Environmental Research Letters*, *11*(12), 124,011. https://doi.org/10.1088/1748-9326/11/12/124011

Zhou, Q., Leng, G., & Huang, M. (2018). Impacts of future climate change on urban flood volumes in Hohhot in northern China: Benefits of climate change mitigation and adaptations. *Hydrology and Earth System Sciences*, *22*(1), 305–316. https://doi.org/10.5194/hess-22-305-2018